Powder Technology 483 (2026) 122838

Contents lists available at ScienceDirect

Powder Technology

journal homepage: www.journals.elsevier.com/powder-technology

Multi-objective inverse identification of meso-scale parameters of bonded particle model of frozen particle systems

Amirali Khosrozadeh [a],*, Amir Khosravifard [b], Swantje Pietsch-Braune [a], Stefan Heinrich [a]

[a] Institute of Solids Process Engineering and Particle Technology, Hamburg University of Technology, Denickestrasse 15, Hamburg, 21073, Hamburg, Germany
[b] Department of Mechanical Engineering, Shiraz University, Shiraz, Iran

GRAPHICAL ABSTRACT

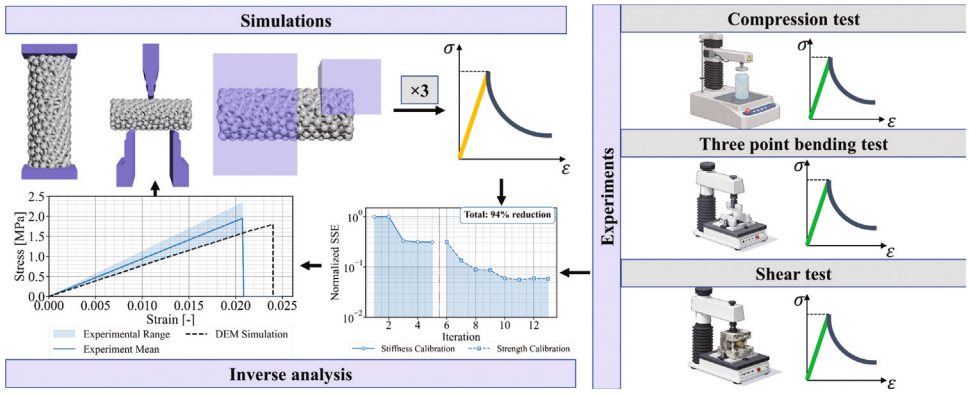

HIGHLIGHTS

- Hybrid global–local inverse identification of meso-scale DEM bond parameters
- Stiffness and strength blocks enable stable Gauss–Newton refinement
- Compression, bending, and shear tests jointly constrain the inverse problem
- Demonstrated on frozen glass beads across multiple temperatures and two loading rates.

ARTICLE INFO

Keywords:
Discrete Element Method (DEM)
Bonded-Particle Model (BPM)
Inverse parameter identification
Multi-objective calibration
Frozen particle-fluid systems

ABSTRACT

Calibrating bond parameters in Bonded-Particle Model (BPM) simulations remains a fundamental challenge due to the mesoscale nature of these parameters. Neither macroscopic mechanical tests nor microscopic characterization techniques can directly measure their properties. Furthermore, the macroscopic response is governed by strongly coupled parameters, leading to non-unique inverse solutions. This study introduces a hybrid inverse calibration framework with Tikhonov regularization based on a scalarized multi-objective formulation that integrates global parameter-space exploration to determine bond parameters. The methodology simultaneously considers uniaxial compression, three-point bending, and shear tests, ensuring consistency across loading modes. The framework is demonstrated on saturated spherical glass-bead specimens as a controlled model

* Corresponding author.
E-mail address: amirali.khosrozadeh@tuhh.de (A. Khosrozadeh).

https://doi.org/10.1016/j.powtec.2026.122838
Received 5 May 2026; Received in revised form 11 June 2026; Accepted 18 June 2026
Available online 29 June 2026

frozen particle system, and is applied across multiple temperatures and two representative loading rates, identifying condition-specific bond-parameter sets whose trends are consistent with the physical behavior of ice bonds.

Nomenclature

Symbol	Description
Bond parameters	
E_b	Young's modulus of ice bonds
d_b	Bond diameter
L_b	Bond length
σ_{max}	Normal (tensile) bond strength
τ_{max}	Tangential (shear) bond strength
A	Creep parameter
m	Creep exponent
Contact parameters	
σ_y	Yield strength
e	Restitution coefficient
μ_s	Sliding friction coefficient
μ_r	Rolling friction coefficient
ϵ_f	Fracture strain
Calibration notation	
$\mathbf{C}$	Full parameter vector
$\mathbf{C}_1$	Block 1 parameters: E_b, d_b, L_b (stiffness block)
$\mathbf{C}_2$	Block 2 parameters: σ_{max}, τ_{max} (strength block)
$Y_i^{(L)}$	Experimental stress value at point i for test L
$U_i^{(L)}$	Simulated stress value at point i for test L
$\sigma_i^{(L)}$	Experimental uncertainty at point i for test L
w_L	Test weight in the objective function
μ_b	Tikhonov regularization parameter for block b
δ_{se}	Finite-difference step size in normalized parameter space
$\mathbf{X}_b$	Sensitivity (Jacobian) matrix for block b
$\mathrm{SSE}(k)$	Sum of squared errors at iteration k
$\widehat{\mathrm{SSE}}(k)$	Normalized SSE at iteration k
Abbreviations	
DEM	Discrete Element Method
BPM	Bonded-Particle Model
DOE	Design of Experiments
LHS	Latin Hypercube Sampling
SSE	Sum of Squared Errors
ANOVA	Analysis of Variance

1. Introduction

The Discrete Element Method (DEM) combined with Bonded-Particle Models (BPM) provides a powerful framework for simulating cohesive granular materials. In these systems, macroscopic mechanical response emerges from particle-scale interactions and progressive bond failure mechanisms [1,2]. In this approach, the granular skeleton is discretized into discrete particles, and cohesive bridges are represented by virtual bonds between neighboring particles. Bond stiffness and strength are prescribed so that bulk stiffness, strength, and failure patterns emerge from particle rearrangement and bond damage rather than being imposed *a priori* [3–5]. This framework has been successfully applied to rocks, concrete, ceramics, and sea ice [2,6,7]. It is particularly relevant for frozen particle-fluid systems (PFS), a class of materials in which pore water solidifies into ice bonds that cement adjacent grains at their contacts. Frozen PFS appear in numerous engineering applications: artificial ground freezing provides temporary excavation support and groundwater control in water-bearing soils [8,9], while similar ice-bonded structures arise in cold-chain storage, cryogenic grinding, and freeze-cast porous materials [10,11]. Depending on loading rate and temperature, frozen PFS can exhibit brittle fracture, ductile yielding, or time-dependent creep, which complicates their mechanical characterization and failure prediction [12,13]. Despite the suitability of DEM-BPM for modeling such systems, a major challenge lies in calibrating bond parameters, as these exist at a mesoscopic scale that is not directly accessible experimentally. [14]. In practice, calibration is therefore performed by trial and error in which bond parameters are manually adjusted until simulated responses approximate experimental measurements [15,16]. This process is tedious, computationally expensive, and dependent on user experience.

Understanding which bond parameters control which macroscopic responses is essential before any calibration can succeed. In DEM-BPM simulations, bond normal and shear stiffnesses largely determine the elastic modulus of the assembly, while bond tensile strength, shear strength, and friction angle together govern peak stress and post-peak softening behavior [2,17]. However, these parameters do not act independently: changing one affects how sensitively the macroscopic response reacts to changes in others, creating a coupled system where isolating individual effects becomes difficult [18]. For frozen PFS, an additional layer of complexity arises from the ice phase itself. Ice bonds are not static; they creep under sustained load and weaken as temperature rises toward the melting point [8]. Consequently, a parameter set calibrated at one strain rate or temperature may fail to predict behavior under different conditions [12,13]. Equally important, different mechanical tests probe different aspects of bond behavior: uniaxial compression emphasizes bond shear and friction, bending activates tensile failure at the outer fiber, and shear isolates the frictional-cohesive response along a predefined plane [19]. A calibration based on a single test type, therefore, risks producing parameters that are valid only for that specific loading mode but perform poorly when the stress state changes.

To move beyond manual trial-and-error, several automated calibration strategies have been developed, which can be broadly grouped into design of experiments (DOE) methods, surrogate models (SMs), optimization methods (OMs), and analytical-computational approaches. DOE methods, such as Taguchi orthogonal arrays and Response Surface Methodology, systematically sample the parameter space and use statistical analysis to identify influential parameters and construct polynomial approximations of the DEM response [15,20,21]. While these techniques reduce blind parameter adjustment, they require a large number of simulation runs to achieve statistical significance, and the sampled points may fail to bracket the true optimum if the design is not sufficiently dense [22]. Surrogate models, using Bayesian optimization, artificial neural networks, and other machine learning methods, address this by learning a continuous mapping from bond parameters to macroscopic outputs, enabling rapid evaluation once the surrogate is trained [23–25]. However, surrogate accuracy depends critically on the number and placement of training samples; in practice, hundreds of DEM simulations are often needed for a single experimental configuration, and the resulting model may exhibit limited transferability to loading conditions outside the training domain [26,27]. Optimization methods treat calibration as minimizing the discrepancy between simulated and experimental responses, employing algorithms such as genetic algorithms, particle swarm optimization, differential evolution, simulated annealing, and other metaheuristic optimizers [28–30], sequential quasi-Monte Carlo filtering [31], Bayesian filtering, and gradient-based solvers [25,32–34]. These methods can locate optimal parameter sets given sufficient iterations, yet most are population-based, requiring many parallel simulations per iteration to update search distributions, which becomes prohibitive for computationally

expensive DEM models [35]. More recently, analytical-computational frameworks have combined sensitivity analysis with gradient optimization: an initial parameter estimate is derived from known physical relationships, and then iteratively refined in a narrow search space until the target accuracy is reached [36,37]. This hybrid strategy reduces the number of required simulations compared to pure black-box search, but existing implementations have focused mainly on elastic calibration or single-test strength matching, and the underlying micro–macro relationships have not been fully exploited during the optimization stage [34].

A deeper difficulty in automated calibration studies is that the inverse problem itself is inherently ill-posed. Because bond parameters interact nonlinearly and different combinations can produce nearly identical macroscopic responses in a given test, the mapping from experiments to parameters is not one-to-one [17,38]. Fitting a single stress–strain curve may therefore yield a parameter set that appears optimal yet fails when the loading mode changes. For example, compression-calibrated parameters frequently overpredict or underpredict bending strength [19]. This non-uniqueness becomes especially problematic for frozen PFS, where rate-dependent and temperature-dependent bond behavior adds further degrees of freedom to an already under-constrained system. As Wang and Tonon [17] pointed out, robust identification requires at least as many independent experimental constraints as there are unknown parameters. Therefore, in this work, it is proposed to combine multiple independent experimental constraints to achieve robust identification of the unknown parameters. As a result, each parameter leaves a distinct signature in at least one measured response. The present work addresses this gap by proposing a hybrid two-phase multi-objective inverse parameter identification framework that couples global parameter space exploration via Latin Hypercube Sampling (LHS) with a Tikhonov-regularized local refinement stage. Three concurrent objectives are pursued by minimizing the discrepancy between simulated and experimental responses from uniaxial compression, three-point bending, and shear tests. Each test activates a fundamentally different failure mechanism, so satisfying all three objectives together constrains the parameter space and reduces the non-uniqueness of the inverse solution, ultimately yielding a physically consistent set of bond parameters for frozen PFS across varying temperatures and strain rates.

2. Materials and test methods

2.1. Materials

The primary granular material used in this study is spherical glass beads. Spherical glass beads were selected as an idealised model material because their nearly monomodal particle-size distribution and regular shape reduce microstructural variability, allowing the calibration framework to be assessed under controlled and reproducible conditions. The particle size distribution (PSD), measured by dynamic image analysis using Camsizer XT, is shown in Fig. 1. The characteristic diameters are $D_{10} = 1615$ μm, $D_{50} = 1688$ μm, and $D_{90} = 1745$ μm, with a span of $(D_{90} - D_{10})/D_{50} = 0.077$, confirming that the glass beads are nearly monomodal.

2.2. Production of test specimens

Specimens were prepared using spherical glass beads, which were saturated with deionized water and frozen under controlled conditions to ensure reproducible ice-bond formation. Frozen specimens were made into flexible silicone molds. Silicone molds enable sample removal without inducing mechanical damage. Deionized water was added slowly from the bottom through a small hole. This bottom-up filling ensures that water infiltrates the pores while air escapes upward, avoiding voids and bubbles. Mild vacuum was applied to remove remaining air and ensure uniform saturation.

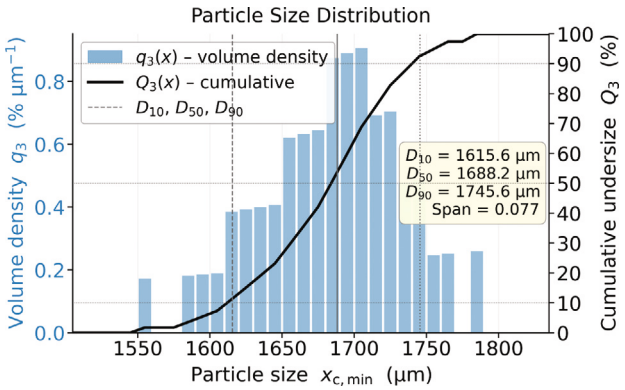

Fig. 1. Particle size distribution of the glass beads.

After filling and degassing, molds were sealed and frozen overnight at −18 °C. Once frozen, specimens were removed from molds and the ends were trimmed with a blade to create flat, parallel surfaces for testing.

The prepared frozen specimens had a nominal length of 25 mm and a diameter of 10 mm, resulting in a slenderness ratio greater than 1.6. This ratio ensured that buckling effects could be neglected during compression and bending tests, so that failure occurred primarily due to material deformation and fracture mechanisms.

2.3. Test procedures

All mechanical tests were conducted at controlled sub-zero temperatures ranging from −5 °Celsius to −15 °Celsius. A self-designed climate chamber, connected to an IKA Temperature Control RC2 basic cryogenic unit (IKA-Werke GmbH & Co. KG, Germany), was used to achieve and maintain stable thermal conditions with minimal deviation. All tests were monitored using a high-speed camera (Series NX-4, Imaging Solutions GmbH, Germany) equipped with a macro lens with 105 mm focal length (Sigma Macro 105 mm F2.8 EX DG OS HSM) to capture crack initiation and propagation behavior. Each test configuration was repeated at least three times for every material type to estimate experimental scatter and construct uncertainty bands for the inverse calibration (Fig. 2).

2.3.1. Uniaxial compression tests

Uniaxial compression tests were conducted to characterize the mechanical response of frozen particle specimens under compressive loading. The displacement-controlled experiments were conducted using a universal Texture Analyzer (T.A.XT Plus, Stable Micro Systems Ltd., Surrey, UK) equipped with a 50 kgf load cell (Fig. 3).

Each specimen was positioned vertically between a rigid metal punch and a fixed base plate. Compression was applied at constant crosshead speeds ranging from 0.01 mm s^{-1} to 1 mm s^{-1} to investigate strain-rate effects. The force–displacement data were recorded continuously until the specimen exhibited complete structural failure or a clear load drop, indicating fracture of the bonded particle network.

2.3.2. Three-point bending tests

Three-point bending tests measured flexural strength and failure of frozen cylindrical specimens. Specimens had the same dimensions as in compression tests (Fig. 4).

Specimens were supported at two points with span length $2L$ = 15 mm, while load was applied at the center at constant displacement rate (Fig. 4(b)). This span length ensures bending stress dominates while minimizing shear at supports.

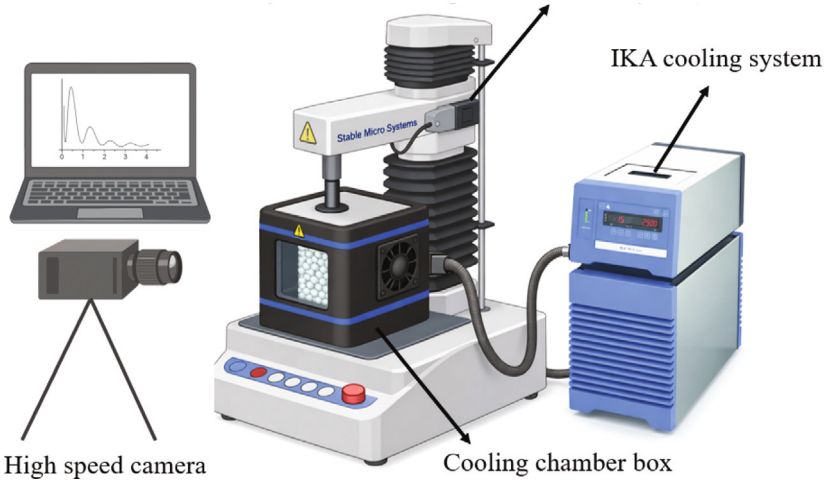

Fig. 2. Schematic of the experimental setup.

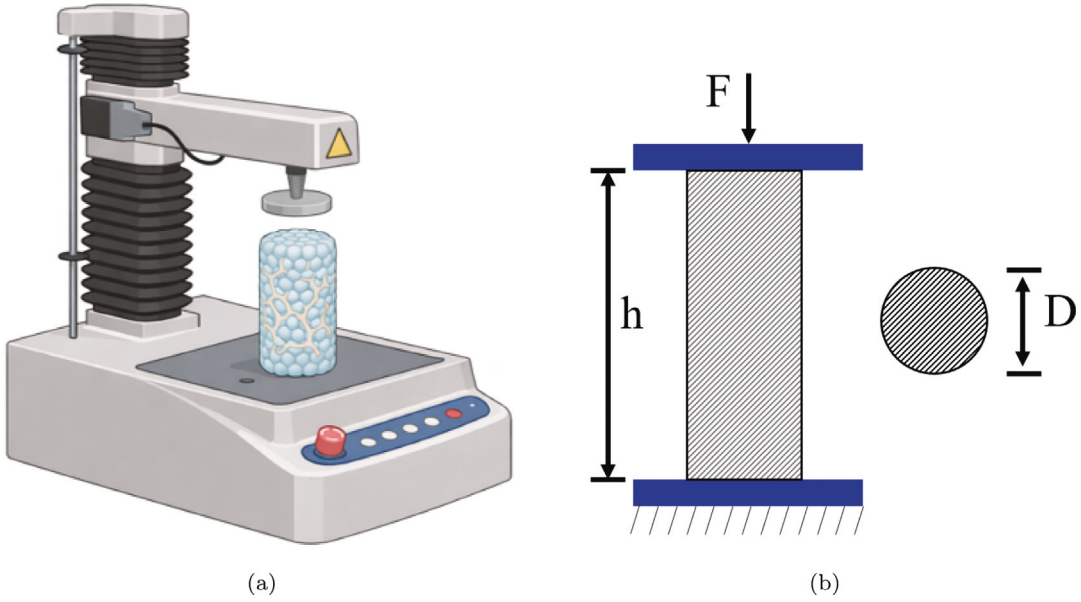

Fig. 3. (a) Compression test device schematic, (b) Schematic diagram.

The flexural stress σ_f for each cylindrical specimen was determined using standard beam theory, which relates the maximum bending stress to the applied bending moment M and the section modulus Z:

$$\sigma_f = \frac{M}{Z} \tag{1}$$

For cylindrical specimens subjected to three-point bending, this relationship can be expressed as:

$$\sigma_f = \frac{Mc}{I} = \frac{32F(2L)}{\pi d^3} = \frac{64FL}{\pi d^3} \tag{2}$$

where F represents the maximum load at fracture, $2L$ denotes the total support span length, and d is the specimen diameter. The corresponding flexural strain at the outer fiber was calculated as:

$$\varepsilon_f = \frac{6\delta d}{(2L)^2} = \frac{3\delta d}{2L^2} \tag{3}$$

where δ is the mid-span deflection measured during the test.

2.3.3. Shear test

The test derives its name from the nature of failure: the specimen is constrained so that fracture occurs along a predefined horizontal plane where shear stress is maximum, isolating the frictional-cohesive response of the ice-bonded granular assembly. Shear tests measured the shear strength of frozen PFS specimens, and a shear box apparatus was installed in the cooling chamber to keep specimens frozen during testing. Before each test, specimens were placed in the pre-cooled shear box to reach thermal equilibrium.

The stainless steel shear box has a horizontal split. The lower half stays fixed while the upper half moves horizontally at constant velocity. A vertical frame applies normal load to hold the specimen and ensure contact at the shear plane. Specimens were carefully aligned to fail along the horizontal shear plane. Petroleum jelly at the box interface reduces friction between apparatus parts.

Tests at low and high strain rates examined loading rate effects on creep behavior typical of ice-rich systems. Normal force was held constant while shear force and displacement were recorded until failure and post-peak behavior (Fig. 5).

Shear stress was calculated as follows:

$$\sigma_s = \frac{f_s}{A_b} \tag{4}$$

where f_s and A_b represent shear force and cross-sectional area, respectively.

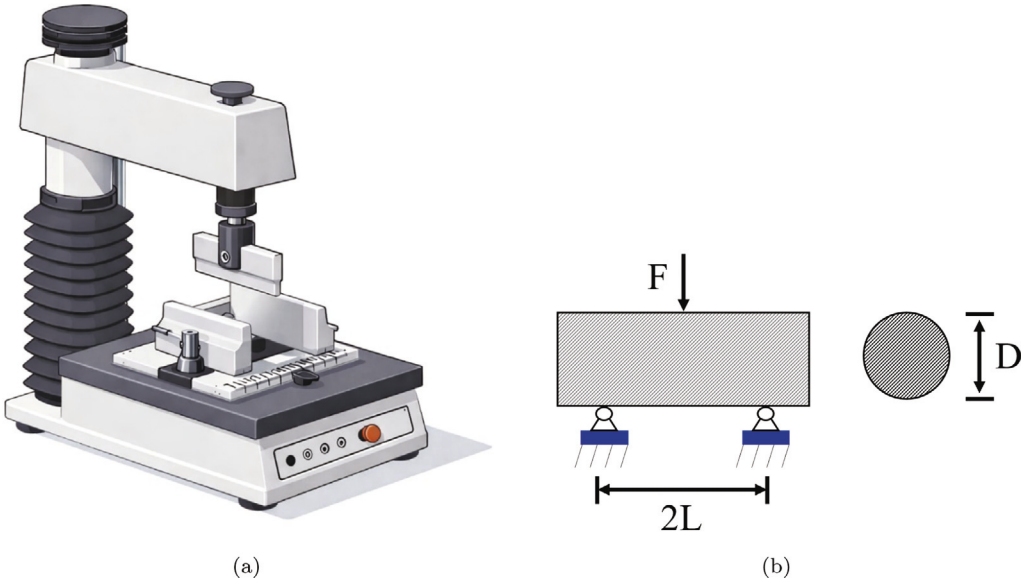

Fig. 4. (a) Three-point bending test device schematic, (b) Schematic diagram.

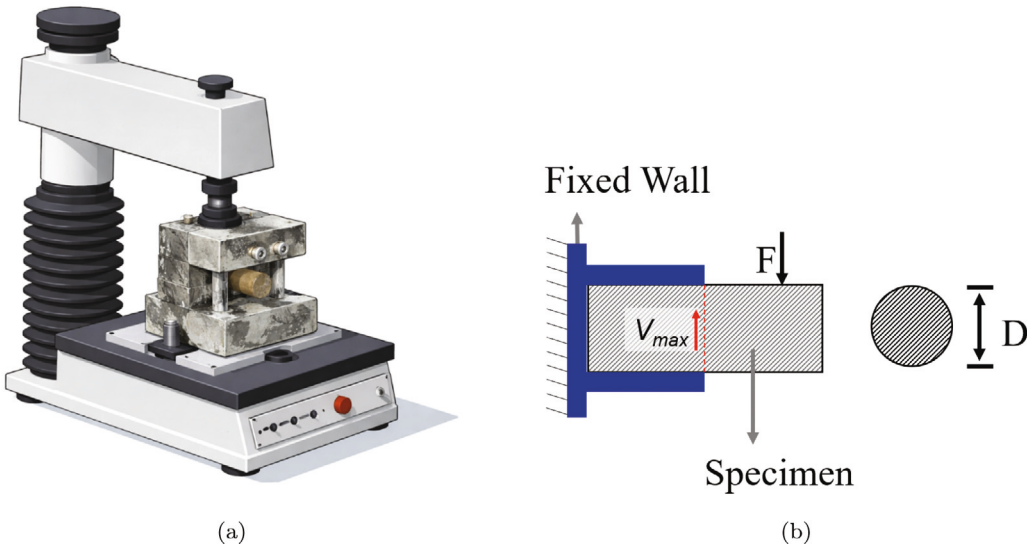

Fig. 5. (a) Test device and specimen, (b) Schematic diagram, where V_{max} denotes the maximum shear displacement.

3. Numerical simulation framework

Frozen PFS mechanical behavior was simulated using DEM with bonded interactions [2,39–41]. All simulations used the open-source GPU-accelerated framework MUSEN [42]. Fig. 6 shows the numerical specimen, an assembly of bonded spherical particles reproducing the geometry of the experimental samples, in the three simulated loading configurations.

3.1. Governing equations and contact model

The translational and rotational motion of every particle i is obtained by integrating Newton's and Euler's equations of motion:

$$m_i \frac{d^2\mathbf{x}_i}{dt^2} = \sum_j \left(\mathbf{F}_{n,ij} + \mathbf{F}_{t,ij}\right) + m_i\mathbf{g}, \tag{5}$$

$$I_i \frac{d\boldsymbol{\omega}_i}{dt} = \sum_j \left(\mathbf{r}_{ij} \times \mathbf{F}_{t,ij} + \mathbf{M}_{r,ij}\right), \tag{6}$$

where m_i, I_i, $\mathbf{x}_i$, and $\boldsymbol{\omega}_i$ are the mass, moment of inertia, position, and angular velocity of particle i; $\mathbf{F}_{n,ij}$ and $\mathbf{F}_{t,ij}$ are the normal and tangential interaction forces with neighbor j; $\mathbf{r}_{ij}$ is the branch vector from the particle centre to the contact point; $\mathbf{M}_{r,ij}$ is the rolling-resistance torque, modelled as a constant directional torque of magnitude $\mu_r R_i|\mathbf{F}_{n,ij}|$ opposing the relative rotation; and $\mathbf{g}$ is the gravitational acceleration.

Non-bonded particle–particle and particle–wall interactions are described by the Hertz–Mindlin model [43]. The normal force superposes a Hertzian elastic term and a viscous damping term:

$$\mathbf{F}_{n,ij} = -\frac{4}{3} E^* \sqrt{R^*}\, \delta_n^{3/2}\, \mathbf{n}_{ij} - \gamma_n \mathbf{v}_{n,ij}, \tag{7}$$

where δ_n is the normal overlap, $\mathbf{n}_{ij}$ the contact unit normal, $\mathbf{v}_{n,ij}$ the normal relative velocity, and γ_n a viscoelastic damping coefficient that is fixed by the restitution coefficient e and the instantaneous normal stiffness rather than prescribed independently. The effective Young's modulus E^* and effective radius R^* are defined as

$$\frac{1}{E^*} = \frac{1-\nu_i^2}{E_i} + \frac{1-\nu_j^2}{E_j}, \qquad \frac{1}{R^*} = \frac{1}{R_i} + \frac{1}{R_j}, \tag{8}$$

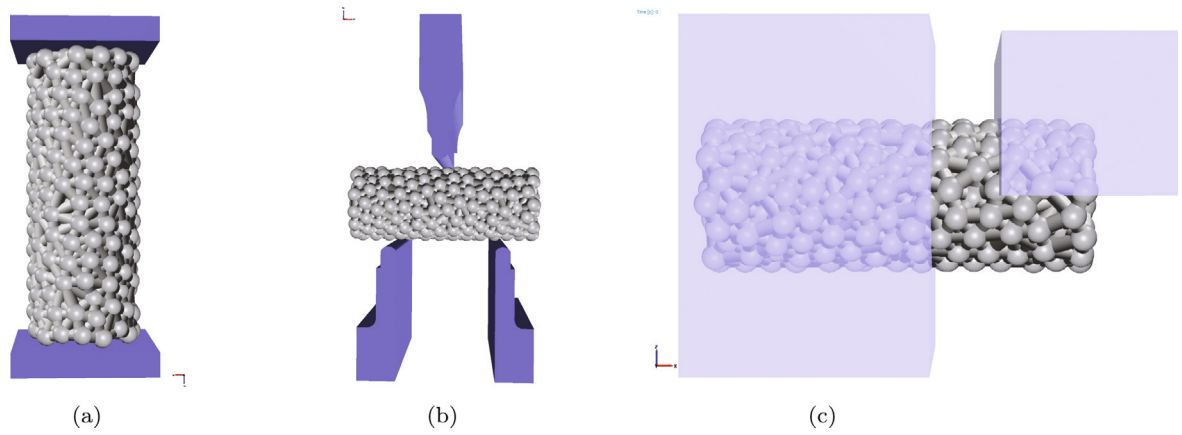

Fig. 6. Numerical DEM specimen of bonded glass beads (grey particles joined by solid bonds) in the three simulated loading configurations: (a) uniaxial compression, (b) three-point bending, and (c) shear. The colored surfaces denote the rigid loading platens and walls.

where E_i, ν_i, and R_i are the Young's modulus, Poisson's ratio, and radius of particle i. The tangential force follows a Mindlin formulation bounded by the Coulomb friction limit:

$$\mathbf{F}_{t,ij} = -\min\left(k_t\,\boldsymbol{\delta}_t,\ \mu_s\,|\mathbf{F}_{n,ij}|\right) - \gamma_t \mathbf{v}_{t,ij}, \tag{9}$$

where $\boldsymbol{\delta}_t$ is the accumulated tangential displacement, $k_t = 8G^*\sqrt{R^*\delta_n}$ the tangential stiffness, G^* the effective shear modulus, μ_s the sliding-friction coefficient, γ_t the tangential damping coefficient, and $\mathbf{v}_{t,ij}$ the tangential relative velocity. The tangential overlap $\boldsymbol{\delta}_t$ is accumulated incrementally with a rigid-body rotation correction and is rescaled when the Coulomb limit $\mu_s|\mathbf{F}_{n,ij}|$ is reached.

Adjacent particles cemented by ice are additionally connected by a cylindrical solid bond of diameter d_b, Young's modulus E_b, Poisson's ratio ν_b, tensile strength σ_{max}, and shear strength τ_{max}. Whereas the Hertz–Mindlin contact governs the unbonded repulsive and frictional response, the solid bond transmits tensile, compressive, shear, and bending loads between bonded particles until it fails, as described next.

3.2. Solid bond model

The solid bond model includes strain-rate dependence and time-dependent creep. Total normal strain $\varepsilon_{n,tot}$ splits into elastic and creep components [40]:

$$\varepsilon_{n,tot} = \varepsilon_{n,el} + \varepsilon_{n,cr} = \frac{L_c - L_0}{L_0} \tag{10}$$

where L_c is the current bond length, L_0 is the initial length, $\varepsilon_{n,el}$ is the elastic strain, and $\varepsilon_{n,cr}$ is the irreversible creep strain. In this model the inelastic deformation is represented entirely by the creep term, which takes the place of a separate plastic strain [40].

The normal stress is:

$$\sigma_n = \begin{cases} E_b \cdot \varepsilon_{n,el} & \text{if } \sigma_n < \sigma_{n,y} \\ \sigma_{n,y} & \text{if } \sigma_n \geq \sigma_{n,y} \end{cases} \tag{11}$$

where $\sigma_{n,y}$ is the yield strength.

The creep strain rate follows Norton's power law:

$$\dot{\varepsilon}_{n,cr} = A \cdot \sigma_n^m \tag{12}$$

The creep exponent m used here reflects that it is a dimensionless effective meso-scale BPM bond exponent, not a directly measured bulk-ice exponent, and A is the corresponding effective bond-level coefficient rather than a bulk single-crystal ice creep constant. The normal bond force is:

$$F_{n,b}(t + \Delta t) = E_b \cdot A_b \cdot [\varepsilon_{n,tot} - \varepsilon_{n,cr}(t + \Delta t)] \tag{13}$$

An analogous formulation governs the tangential direction. The tangential bond deformation $\boldsymbol{\delta}_t$ is accumulated incrementally with a rigid-body rotation correction, giving a tangential bond stress and force

$$\tau = \frac{|\boldsymbol{\delta}_t|}{L_0}\,\frac{E_b}{2(1+\nu_b)}, \qquad \mathbf{F}_{t,b} = \frac{E_b}{2(1+\nu_b)}\,A_b\,\frac{\boldsymbol{\delta}_t}{L_0}, \tag{14}$$

with a tangential creep contribution accumulated using the same power law as in the normal direction. A bond fails and is removed from the simulation when either strength limit is exceeded, with the bending and torsional bond moments contributing to the respective stresses [40]:

$$\frac{|\mathbf{F}_{n,b}|}{A_b} + \frac{|\mathbf{M}_{n,b}|\,R_b}{I} \geq \sigma_{max}, \qquad \frac{|\mathbf{F}_{t,b}|}{A_b} + \frac{|\mathbf{M}_{t,b}|\,R_b}{J} \geq \tau_{max}, \tag{15}$$

where $\mathbf{M}_{n,b}$ and $\mathbf{M}_{t,b}$ are the bending and torsional bond moments, R_b is the bond radius, and I and J are the area and polar moments of inertia of the bond cross-section. The calibrated strength parameters σ_{max} and τ_{max} enter the model through these two criteria.

3.3. Time step analysis

Time step was determined from the Rayleigh time criterion for stability in explicit integration. For bonded particle systems with high stiffness, time step was set to one-tenth of the Rayleigh time step:

$$\Delta t = 0.1 \times \pi R_{min}\sqrt{\frac{\rho}{G}} \cdot \frac{1}{0.1631\nu + 0.8766} \tag{16}$$

where R_{min}, ρ, G, and ν are the minimum particle radius, density, shear modulus, and Poisson's ratio, respectively. All simulations used $\Delta t = 1 \times 10^{-8}$ s.

4. Parameter identification framework

4.1. Design of Experiments (DOE)

Before beginning the calibration process, it is essential to identify the material parameters that have the greatest influence on the mechanical response of frozen PFS. Moreover, understanding these parameters reduces the dimensionality of the optimization.

A Taguchi L_{32} orthogonal array explored parameter space with low computational cost [44]. This design evaluated ten parameters at four levels each using only 32 runs instead of $4^{10} = 1{,}048{,}576$ for full factorial. Three tests of compression, bending, and shear were simulated for each combination, and analysis of variance (ANOVA) quantified the statistical significance of each parameter's effect on maximum force and stiffness.

From the results of the ANOVA in Appendix A, five parameters are statistically significant in all three tests. These parameters, which are given in Table 1, were chosen for inverse identification because

Table 1
Statistical significance of all investigated parameters across three mechanical tests.

Parameter	Symbol	Compression	Shear	Bending
Selected for inverse identification:				
Young's modulus	E_b	**	**	**
Normal strength	σ_{max}	***	–	*
Tangential strength	τ_{max}	**	–	–
Creep parameter	A	*	***	***
Creep exponent	m	–	***	***

*** Significance: $p < 0.01$
** Significance: $p < 0.05$
* Significance: $p < 0.10$
– not significant

they consistently influence the mechanical response and are physically meaningful. In addition to these five parameters, two structural parameters have been considered (Section 4.3).

The selection of these five parameters was further supported by examining their physical interpretability and mutual independence. The Young's modulus (E_b) and the two strength parameters (σ_{max} and τ_{max}) represent fundamental material properties that can be independently varied without introducing physical inconsistencies. The two creep parameters (A and m) together describe the viscoplastic constitutive behavior, with A controlling the overall creep magnitude and m governing its nonlinearity. This parameterization ensures that the inverse problem seeks physically meaningful combinations rather than arbitrary fitting coefficients.

4.2. Global parameter space exploration

Parameter identification is formulated as a scalarised multi-objective inverse problem in which the discrepancies of the three mechanical tests are combined into a single weighted-sum objective. Before conducting the local inverse analysis, a global exploration of the parameter space was performed using Latin Hypercube Sampling (LHS) [45] to identify an initial region for optimization. This global search phase provides initial parameter estimates that are not excessively distant from the true solution, thereby improving convergence behavior of the subsequent local optimization.

A total of $N_{LHS} = 50$ parameter combinations were sampled, covering all five parameters that affect mechanical response. For each parameter combination, DEM simulations of all three mechanical tests were executed, and the overall objective function was evaluated by comparing simulated and experimental stress–strain curves.

The objective function for the global search was formulated as the weighted sum of squared residuals across all three tests:

$$S_{global}(\mathbf{C}) = \sum_{L=1}^{3} w_L \sum_{i=1}^{N_L} \left[\frac{Y_i^{(L)} - U_i^{(L)}(\mathbf{C})}{\sigma_i^{(L)}} \right]^2 \tag{17}$$

where w_L are test-level scalar weights, $Y_i^{(L)}$ represents experimental stress values, $U_i^{(L)}(\mathbf{C})$ represents simulated stress values, and $\sigma_i^{(L)}$ represents local experimental uncertainty. The three mechanical tests are treated as equally important experimental constraints because compression, bending, and shear probe different mechanical responses of the same bonded material. In this study w_L was therefore set to unity for all three tests, so that no loading mode is given priority over another, and the calibrated bond-parameter set is jointly consistent with all three responses. The weights are nevertheless retained in the formulation so that future applications can emphasize specific loading modes if required. The test-level weights w_L should be distinguished from the point-wise weighting matrix $\mathbf{W}$ used in the local refinement (Section 4.3).

The best parameter sets from LHS (those with $S_{global} < S_{threshold}$, where $S_{threshold}$ is the 5th percentile) were analyzed to determine values for the creep parameters. The DOE study (Section 4.1) showed that A and m have strong global sensitivity over their full ranges, but the LHS database also showed that only a limited region of A and m values produced numerically stable DEM simulations together with responses close to the experimental curves. Across the investigated temperatures and loading rates, the same stable pair was therefore consistently selected from the global search. Fixing A and m at these screened values during local refinement is a deliberate identifiability and stability choice; it is not an assumption that meso-scale creep is temperature-independent.

Local insensitivity creates problems for gradient-based inverse analysis. Locally insensitive parameters contribute little to the sensitivity matrix (Jacobian), causing ill-conditioning and instability, while inappropriate creep values can destabilize the DEM simulation through unphysical deformation or premature failure. Local finite-difference perturbations of A and m around the stable region did not produce reliable, monotonic response changes suitable for Gauss–Newton updating, so these parameters are excluded from the local Jacobian computation.

Global search provides: (1) initial estimates for E_b, d_b, L_b, σ_{max}, and τ_{max} in a promising parameter region, used both as starting points and as priors in the Tikhonov term of the local refinement; (2) fixed, realistic values for A and m that keep DEM simulations stable during local refinement.

4.3. Local refinement phase: Alternating block minimization

The local refinement phase uses alternating block minimization by partitions the parameters into two physically motivated blocks based on their dominant sensitivities and optimizes them sequentially, making each local sub-problem better conditioned than the joint optimization of all parameters at once.

The parameters are partitioned as follows:

$$\mathbf{C} = \begin{bmatrix} \mathbf{C}_1 \\ \mathbf{C}_2 \end{bmatrix} = \begin{bmatrix} E_b, d_b, L_b \\ \sigma_{max}, \tau_{max} \end{bmatrix} \tag{18}$$

where $\mathbf{C}_1$ collects the stiffness-dominant parameters (Block 1) and $\mathbf{C}_2$ collects the strength-dominant parameters (Block 2). The partition is based on dominant parameter sensitivities rather than strict independence. Stiffness parameters can also affect peak stress through force transmission and bond loading, while strength parameters can affect the pre-peak response once local bond damage initiates, so the two blocks are weakly coupled. The alternating strategy therefore reduces the dimensionality of each local update for numerical stability, but the objective function always includes the full residual over compression, bending, and shear; the cross-coupling is handled iteratively, since each block update is followed by re-optimization of the other block in the next outer iteration.

4.3.1. Bond diameter domain estimation for block 1

Block 1 parameters (E_b, d_b, L_b) are strongly coupled in their effects on specimen stiffness. Cantilever beam bending tests estimated a valid search domain for d_b to ensure realistic bounds and reasonable initial guesses.

Cantilever beam tests were performed on frozen PFS specimens. Specimens were clamped at one end with forces of 5 N, 10 N, and 15 N applied at the free end. Compliance (displacement per unit force) was measured for each load, and it was repeated five times [46].

Deflection was analyzed using Timoshenko beam theory, which includes both bending and shear deformation. This is needed because specimens have a small slenderness ratio ($L/h < 10$), making the Euler–Bernoulli theory inadequate since it ignores shear deflection. Total deflection from Timoshenko theory is:

$$\delta = \frac{FL^3}{3EI} + \frac{FL}{kGA} \tag{19}$$

where F is applied force, L is beam length, E is Young's modulus, I is second moment of area, k is shear correction factor, G is shear

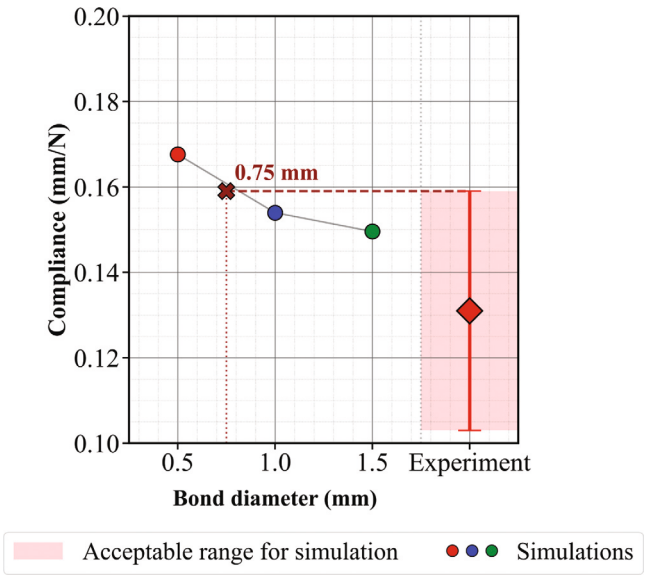

Fig. 7. Bond Diameter Domain Estimation.

modulus, and A is cross-sectional area. For circular cross-sections, $k = 6(1+\nu)/(7+6\nu) \approx 0.9$ and $G = E/(2(1+\nu))$.

Bond strength was set very high in simulations to eliminate bond failure and isolate elastic deformation, so only elastic compliance controls the response. Three d_b values were tested, i.e. 0.5 mm, 1.0 mm, and 1.5 mm, giving different stiffness.

Fig. 7 compares experimental compliance with DEM results for the three d_b values. Each simulation ran three times with negligible differences in elastic zone. Results show d_b more than around 0.75 mm reproduces experimental compliance when combined with appropriate E_b and L_b.

From this study, realistic d_b search domains were set for each material.

This domain estimation procedure establishes physically realistic bounds.

4.3.2. Multi-test objective function

For each test type L (where $L = 1$ for compression, $L = 2$ for bending, and $L = 3$ for shear), stress–strain data at N_L measurement points are collected. The vector of measured stress for test L is denoted $\mathbf{Y}^{(L)}$, and the corresponding simulated stresses are $\mathbf{U}^{(L)}(\mathbf{C}_1, \mathbf{C}_2)$.

Combining data from all three tests, the complete measurement and simulation vectors are:

$$\mathbf{Y} = \begin{bmatrix} \mathbf{Y}^{(1)} \\ \mathbf{Y}^{(2)} \\ \mathbf{Y}^{(3)} \end{bmatrix}, \quad \mathbf{U}(\mathbf{C}_1, \mathbf{C}_2) = \begin{bmatrix} \mathbf{U}^{(1)}(\mathbf{C}_1, \mathbf{C}_2) \\ \mathbf{U}^{(2)}(\mathbf{C}_1, \mathbf{C}_2) \\ \mathbf{U}^{(3)}(\mathbf{C}_1, \mathbf{C}_2) \end{bmatrix} \tag{20}$$

The local refinement uses a prior-based Tikhonov regularization [47] together with an envelope-aware data-misfit term to solve this ill-posed inverse problem. For each measurement point i in test L, a signed envelope-aware residual is defined as

$$r_{\text{env},i}^{(L)} = \begin{cases} 0 & \text{if } Y_{\text{lower},i}^{(L)} \le U_i^{(L)} \le Y_{\text{upper},i}^{(L)}, \\ Y_{\text{upper},i}^{(L)} - U_i^{(L)} & \text{if } U_i^{(L)} > Y_{\text{upper},i}^{(L)}, \\ Y_{\text{lower},i}^{(L)} - U_i^{(L)} & \text{if } U_i^{(L)} < Y_{\text{lower},i}^{(L)}, \end{cases} \tag{21}$$

where $[Y_{\text{lower},i}^{(L)}, Y_{\text{upper},i}^{(L)}]$ is the experimental scatter envelope at point i of test L. The point-wise weighted residual vector used in the local refinement is

$$\mathbf{r}_w = \mathbf{W}\,\mathbf{r}_{\text{env}}, \tag{22}$$

where $\mathbf{W}$ is a diagonal point-wise weighting matrix that emphasizes the elastic/pre-peak and peak regions and de-emphasizes the more variable post-peak region. Because the three loading modes are weighted equally in the present study, consistent with the global objective (Eq. (17)) in which $w_L = 1$, the test-level weights reduce to unity and $\mathbf{W}$ is the only weighting applied during the local refinement; the same matrix premultiplies the rows of the sensitivity matrix $\mathbf{X}_b$, so that the Gauss–Newton update (Eq. (30)) remains consistent. This formulation treats all simulations within the experimental scatter band as equally acceptable and penalizes only deviations outside the measured envelope.

The block-specific objective functions are then

$$S_1(\mathbf{C}_1 \mid \mathbf{C}_2) = \mathbf{r}_w^T \mathbf{r}_w\Big|_{\mathbf{C}_2=\mathbf{C}_2^{\text{fixed}}} + \mu_1(\mathbf{C}_1 - \mathbf{C}_1^{\text{prior}})^T(\mathbf{C}_1 - \mathbf{C}_1^{\text{prior}}), \tag{23}$$

$$S_2(\mathbf{C}_2 \mid \mathbf{C}_1) = \mathbf{r}_w^T \mathbf{r}_w\Big|_{\mathbf{C}_1=\mathbf{C}_1^{\text{fixed}}} + \mu_2(\mathbf{C}_2 - \mathbf{C}_2^{\text{prior}})^T(\mathbf{C}_2 - \mathbf{C}_2^{\text{prior}}), \tag{24}$$

where μ_1 and μ_2 are block-specific regularization parameters, $\mathbf{C}_b^{\text{prior}}$ is the corresponding block estimate obtained from the global LHS search of Section 4.2, and the superscript "fixed" indicates parameters held constant during that block's optimization. The Tikhonov term penalizes deviations from the global-search prior and stabilizes the local inverse problem without biasing physically non-zero parameters toward zero. The prior-based Tikhonov term is applied in the same log-transformed and normalized parameter space used for the local update so that no parameter is artificially favored by its physical scale.

4.4. Inverse method algorithm

The inverse approach determines the unknown parameters by minimizing the discrepancy between simulated and experimental responses through a Tikhonov-regularised damped Gauss–Newton procedure [48, 49], where the same step-length damping strategy has been used in previous inverse-identification work. Starting from the initial estimates $\mathbf{C}_1^0$ and $\mathbf{C}_2^0$ obtained from the global search (Section 4.2), which also serve as the priors $\mathbf{C}_1^{\text{prior}}$ and $\mathbf{C}_2^{\text{prior}}$, the algorithm alternates between updating Block 1 and Block 2 until convergence is achieved for both blocks. At outer iteration n, the algorithm performs:

Step 1: Update Block 1 (Stiffness parameters)

Fix $\mathbf{C}_2 = \mathbf{C}_2^n$ and solve for $\mathbf{C}_1^{n+1}$ by minimizing $S_1(\mathbf{C}_1 \mid \mathbf{C}_2^n)$ using the Tikhonov-regularized damped Gauss–Newton method. The simulated response is linearized around the current estimate $\mathbf{C}_1^{n,k}$ at inner iteration k:

$$\mathbf{U}(\mathbf{C}_1, \mathbf{C}_2^n) \approx \mathbf{U}^{n,k} + \mathbf{X}_1^{n,k}(\mathbf{C}_1 - \mathbf{C}_1^{n,k}) \tag{25}$$

where $\mathbf{X}_1^{n,k}$ is the sensitivity matrix containing derivatives of simulated stress with respect to Block 1 parameters only:

$$\mathbf{X}_1 = \begin{bmatrix} \mathbf{X}_1^{(1)} \\ \mathbf{X}_1^{(2)} \\ \mathbf{X}_1^{(3)} \end{bmatrix}, \quad (X_1)_{ij}^{(L)} = \frac{\partial U_i^{(L)}}{\partial (C_1)_j}, \quad j \in \{E_b, d_b, L_b\} \tag{26}$$

Step 2: Update Block 2 (Strength parameters)

Fix $\mathbf{C}_1 = \mathbf{C}_1^{n+1}$ and solve for $\mathbf{C}_2^{n+1}$ by minimizing $S_2(\mathbf{C}_2 \mid \mathbf{C}_1^{n+1})$ using the same Tikhonov-regularized damped Gauss–Newton method. Similarly, the linearization is:

$$\mathbf{U}(\mathbf{C}_1^{n+1}, \mathbf{C}_2) \approx \mathbf{U}^{n,k} + \mathbf{X}_2^{n,k}(\mathbf{C}_2 - \mathbf{C}_2^{n,k}) \tag{27}$$

where $\mathbf{X}_2^{n,k}$ is the sensitivity matrix for Block 2 parameters:

$$\mathbf{X}_2 = \begin{bmatrix} \mathbf{X}_2^{(1)} \\ \mathbf{X}_2^{(2)} \\ \mathbf{X}_2^{(3)} \end{bmatrix}, \quad (X_2)_{ij}^{(L)} = \frac{\partial U_i^{(L)}}{\partial (C_2)_j}, \quad j \in \{\sigma_{max}, \tau_{max}\} \tag{28}$$

Sensitivity coefficients are computed using forward finite differences in the normalized parameter space $\tilde{\mathbf{C}}_b \in [0,1]^{n_b}$:

$$(X_b)_{ij}^{(L)} = \frac{U_i^{(L)}(\tilde{C}_{b,j} + \delta_{se,j}) - U_i^{(L)}(\tilde{C}_{b,j})}{\delta_{se,j}}, \quad b \in \{1,2\} \tag{29}$$

where $\tilde{C}_{b,j}$ is the jth normalized parameter of block b and $\delta_{se,j}$ is the absolute perturbation step in normalized space for that parameter. Using an absolute step in normalized space ensures equal relative resolution across parameters with different physical scales and avoids vanishing perturbations near zero. The step sizes are selected per parameter based on the sensitivity analysis (Section 5.2): $\boldsymbol{\delta}_{se} = [0.05, 0.05, 0.05]$ for Block 1 (E_b, d_b, L_b) and $\boldsymbol{\delta}_{se} = [0.05, 0.15]$ for Block 2 (σ_{max}, τ_{max}), balancing truncation error against DEM simulation noise.

For each block $b \in \{1,2\}$, minimizing the respective objective function (Eqs. (23) or (24)) with respect to $\mathbf{C}_b$ and applying the linearization yields the prior-regularized Gauss–Newton search direction. Throughout, the residual is defined with the sign convention $\mathbf{r}_w = \mathbf{W}\,\mathbf{r}_{\text{env}}$, with $r_{\text{env},i}$ as in Eq. (21). The block update is

$$\Delta\mathbf{C}_b = \left[(\mathbf{X}_b^{n,k})^T\mathbf{X}_b^{n,k} + \mu_b^{n,k}\mathbf{I}\right]^{-1}\left[(\mathbf{X}_b^{n,k})^T\mathbf{r}_w^{n,k} - \mu_b^{n,k}(\mathbf{C}_b^{n,k} - \mathbf{C}_b^{\text{prior}})\right], \tag{30}$$

$$\mathbf{C}_b^{n,k+1} = \mathbf{C}_b^{n,k} + \alpha\,\Delta\mathbf{C}_b, \tag{31}$$

where α is a scalar step length introduced for nonlinear globalization. After computing the Tikhonov-regularized Gauss–Newton search direction, the trial update is multiplied by α, which is initialized as $\alpha = 1$ at the start of each inner iteration. If the objective S_b decreases, the update is accepted; if it does not decrease, α is repeatedly halved ($\alpha \leftarrow \alpha/2$) until a decrease is obtained or a prescribed lower bound on α is reached, in which case the inner iteration is terminated. Thus, μ_b controls the regularization of the inverse problem, whereas α controls acceptance of the nonlinear update; the two stabilizing mechanisms act independently.

The inner iteration k continues until block-level convergence:

$$\|\mathbf{C}_b^{n,k+1} - \mathbf{C}_b^{n,k}\| \le \epsilon_{block}, \tag{32}$$

evaluated in the log-transformed and normalized parameter space. Block-level convergence is satisfied when all active parameters in the block change by less than 1% between two successive inner iterations, i.e. ϵ_{block} corresponds to a 1% normalized relative-change criterion rather than a tolerance in physical units.

The outer BCD loop alternates between Block 1 and Block 2 updates and stops when *any* of the following criteria is satisfied, all evaluated in the same transformed and normalized parameter space:

1. the relative change of every normalized parameter between two successive iterations is below 1%;
2. the relative change in the weighted SSE between two successive iterations is below 10^{-3};
3. the weighted SSE itself is below 10^{-2};
4. the envelope coverage reaches at least 95% for all three tests, where envelope coverage is the fraction of simulation points lying inside the experimental uncertainty envelope.

The criteria are checked after each outer iteration; satisfying any one of them terminates the outer loop.

Several enhancements improve numerical stability. Parameters spanning multiple orders of magnitude are transformed to logarithmic space ($\log_{10}$) before optimization, improving conditioning. All parameters are normalized to $[0,1]$ using their bounds for dimensionless optimization. The data-misfit term uses the envelope-aware weighted residual of Eqs. (21)–(22), so that simulation points within the experimental uncertainty band contribute zero residual while deviations outside the envelope are penalized by their distance from the nearest boundary, weighted point-wise by $\mathbf{W}$.

Each column of $\mathbf{X}_b$ is normalized by its Euclidean norm before solving the Tikhonov-regularized update of Eq. (30); this balances parameters with different sensitivities and reduces the condition number of $\mathbf{X}_b^T\mathbf{X}_b + \mu_b\mathbf{I}$ by 2–3 orders of magnitude.

Table 2
Parameter bounds for inverse analysis and LHS.

Block	Parameter	Lower Bound	Upper Bound	Unit
Block 1 (Stiffness)	E_b	5	50	MPa
	d_b	0.75	1.5	mm
	L_b	0.01	5	mm
Block 2 (Strength)	σ_{max}	1	50	MPa
	τ_{max}	0.1	10	MPa

4.5. Selection of regularization parameter

The regularization parameter μ_b is not fixed manually. At each inner iteration it is selected from the candidate grid

$$\mu_b \in \{10^{-4}, 10^{-2}, 10^{-1}, 1, 10\} \tag{33}$$

in the log-transformed and normalized parameter space, after Jacobian column scaling. Candidate values are tested in turn and the value producing the smallest predicted weighted-residual norm is selected. If the resulting regularized normal system remains ill-conditioned, defined here by $\text{cond}(\mathbf{X}_b^T\mathbf{X}_b + \mu_b\mathbf{I}) > 10^{10}$, the next larger μ_b value from the grid is used. Across the calibrations reported here, the selected μ_b values remained inside the candidate grid and ranged from 10^{-4} to 1.

4.6. Parameter bounds

Parameter search space was constrained to physically realistic ranges (Table 2). For Block 1, bond diameter bounds come from cantilever beam tests (Section 4.3.1), while E_b and L_b reflect literature values for ice at sub-zero temperatures [40].

For Block 2 strength parameters, bounds accommodate variability in ice bond strength from temperature, porosity, and microstructure. Normal and tangential strength span wide ranges to explore the full spectrum of brittle to ductile behavior.

Figs. 8 and 9 present the complete flowchart representation of the block coordinate descent inverse analysis algorithm. Fig. 8 illustrates the outer alternating minimization loop, showing the global search initialization and the sequential optimization of stiffness and strength parameters. Moreover, Fig. 9 presents the detailed flowchart for the inner Gauss–Newton iterations performed within each block optimization.

5. Results and discussion

5.1. Experimental observations: Strain rate and temperature effects

Experimental tests were conducted at two displacement speeds (0.01, 0.1, and 1 mm s^{-1}) and multiple temperatures to characterize the rate- and temperature-dependent behavior of frozen PFS. Two of these speeds, 0.01 and 1 mm s^{-1}, were used as representative low- and high-rate calibration cases in Section 5.3. Fig. 10 shows that increasing displacement speed consistently raises both elastic modulus and maximum stress across all three loading modes. This trend arises because at higher strain rates the material cannot relax fast enough to accommodate deformation, so the ice bonds resist more and behave more stiffly, requiring higher stress for the same strain and producing a higher apparent modulus. At lower strain rates, in contrast, microcracks have time to partially close before propagating, which reduces the overall resistance and leads to a softer, lower-strength response.

Temperature acts through a closely related mechanism. As shown in Fig. 11, reducing temperature from −5 °Celsius to −15 °Celsius increases both elastic modulus and maximum stress across all test types, mirroring the strain-rate trend. At lower temperatures, atomic and molecular mobility is reduced. Therefore, atoms vibrate less and remain closer to their equilibrium positions, making interatomic bonds

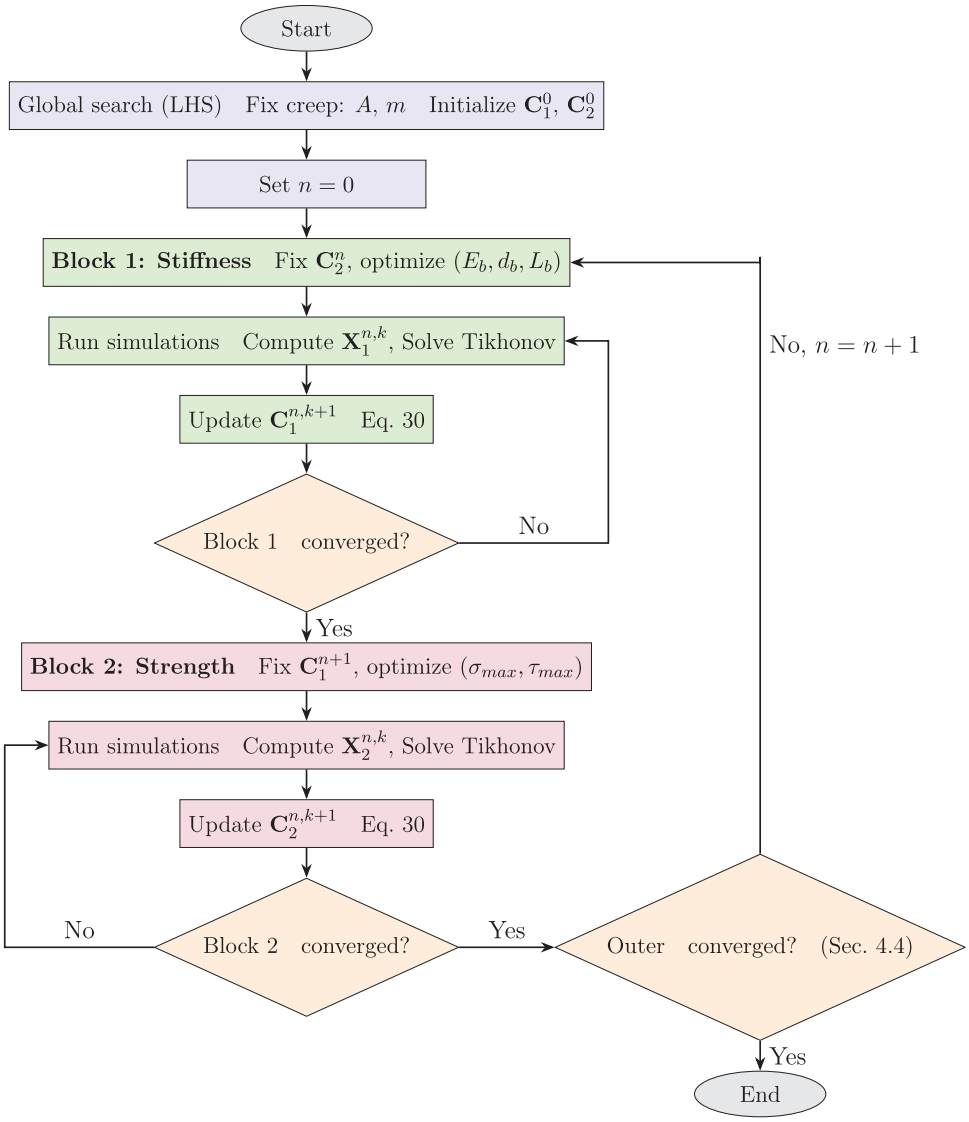

Fig. 8. Flowchart of the block coordinate descent.

more resistant to deformation. Together, these two sets of observations are consistent with viscoplastic behavior of the ice-bonded network. In the present inverse model, however, the creep parameters are treated as stability-controlling parameters fixed from the global search, while the condition-specific changes are mainly represented through the calibrated stiffness and strength parameters; the calibration framework must therefore account for both dependencies through condition-specific parameter sets rather than through a temperature- or rate-dependent creep law.

The scatter in the experimental data is notably higher at elevated strain rates, where brittle fracture is more abrupt and less reproducible than the quasi-ductile failure observed at lower rates. Specimen-to-specimen variability is further amplified by residual air voids and micro-cracks that can remain entrapped during specimen preparation despite ultrasonic treatment, promoting premature local failure under high-rate loading.

5.2. Simulation parameters sensitivity analysis

Beyond confirming the DOE parameter ranking, the manual sensitivity analysis serves the purpose of selecting the finite-difference step size δ_{se} used to compute the Jacobian.

Figs. 12 and 13 show the response when each of the five locally identifiable parameters (E_b, d_b, L_b, σ_{max}, τ_{max}) is varied individually. The response changes smoothly and proportionally with the parameter perturbation, which is the condition required for a well-conditioned finite-difference Jacobian. Based on these graphs, a step size of $\delta_{se} = 5\%$ of the normalized parameter range was selected for Block 1 (E_b, d_b, L_b), and $\delta_{se} = 5\%$ and 15% for σ_{max} and τ_{max}, respectively, in Block 2, balancing the truncation error against the DEM simulation noise. Parameters with negligible influence, confirmed by the flat overlapping curves in Fig. 14, are excluded from the optimization entirely.

5.3. Inverse calibration results

5.3.1. Temperature-dependent calibration

Fig. 15 presents the calibrated stress–strain curves at $T = -15$ °Celsius, showing DEM simulation results alongside experimental measurements. The simulation curves fall within or close to the experimental uncertainty bands across all three loading modes. Similarly, it was obtained at $T = -10$ °Celsius and $T = -5$ °Celsius, as presented in Figs. 16 and 17.

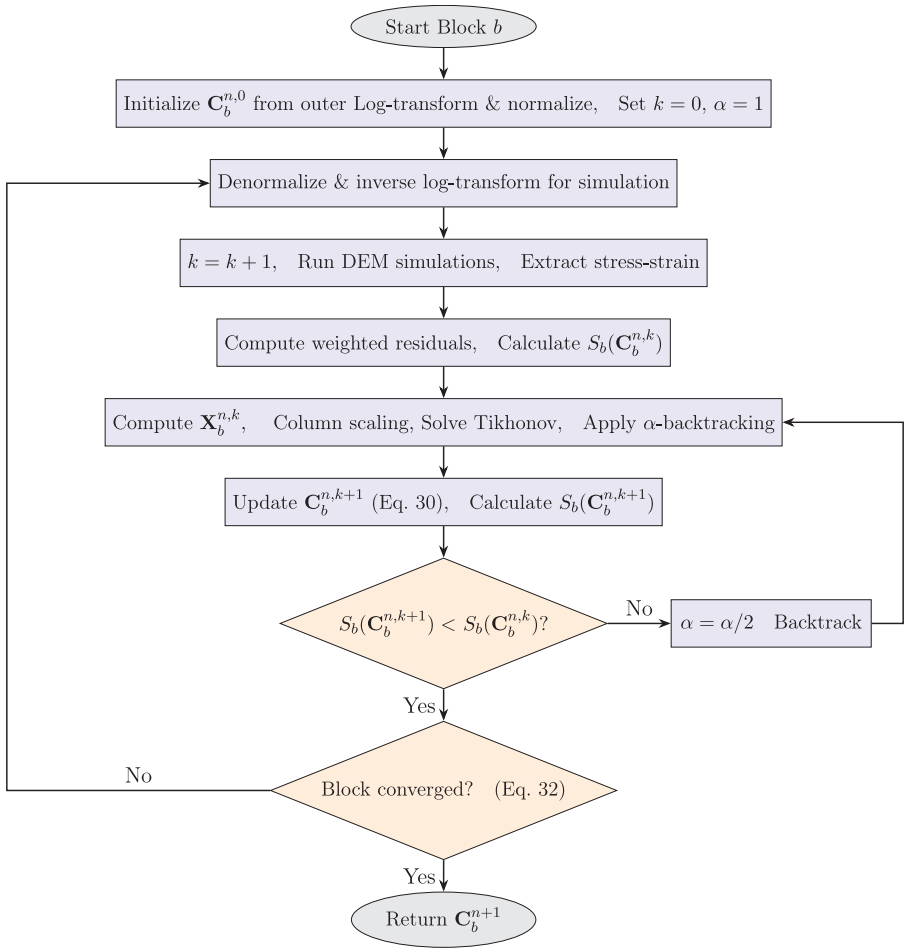

Fig. 9. Detailed flowchart for the inner Gauss–Newton iterations within each block optimization ($b \in \{1, 2\}$).

To convergence, the SSE at iteration k is evaluated as the weighted sum of squared residuals across all three tests:

$$\mathrm{SSE}(k) = \sum_{L=1}^{3} w_L \sum_{i=1}^{N_L} \left[\frac{Y_i^{(L)} - U_i^{(L)}(\mathbf{C}^{(k)})}{\sigma_i^{(L)}} \right]^2, \tag{34}$$

where $\mathbf{C}^{(k)}$ denotes the parameter vector at iteration k, consistent with the objective function defined in Eq. (17). The normalized SSE is then:

$$\widehat{\mathrm{SSE}}(k) = \frac{\mathrm{SSE}(k)}{\mathrm{SSE}(1)}, \tag{35}$$

where SSE(1) is the value at the highest value of each phase, so $\widehat{\mathrm{SSE}}(1) = 1$ by construction.

Fig. 18 summarizes the convergence of $\widehat{\mathrm{SSE}}$ across all iterations for each temperature. Two distinct optimization phases are visible in each panel. The first is stiffness calibration, located at the left of the dashed vertical line, which reduces the elastic mismatch by updating E_b, d_b, and L_b. The second one, strength calibration, targets peak stress and failure behavior through σ_{max} and τ_{max}. At $T = -15$ °Celsius and $T = -10$ °Celsius, the two-phase procedure achieves total SSE reductions of 94% and 95%, respectively, demonstrating efficient convergence. At $T = -5$ °Celsius, the reduction is 28%, which reflects the benefit of prior knowledge accumulated from the two preceding calibrations. Since only temperature differs between cases, the parameters identified at $T = -15$ and $T = -10$ °Celsius provide a close initial estimate for $T = -5$ °Celsius, placing the starting point already near the optimum and requiring only a small number of iterations to reach a better solution. The smaller percentage reduction at $T = -5$ °Celsius therefore reflects that the initial parameter set was already close to the final calibrated solution, rather than indicating a poorer final fit. In terms of computational effort, the refinement converged within 13, 32, and 14 optimization iterations at $T = -15$, -10, and -5 °Celsius, respectively (Fig. 18), where each iteration evaluates the full three-test objective function.

Table 3 lists the optimized bond parameters identified by the inverse algorithm for all four calibration cases. These are the parameter sets whose corresponding simulated stress–strain curves are shown in Figs. 15–17 for the temperature variation cases and in Fig. 19 for the strain-rate variation case.

As indicated by the table, the creep parameters A and m were selected from the global LHS search and kept fixed during local block refinement because they controlled numerical stability and were not locally identifiable for Gauss–Newton updating.

5.3.2. Strain-rate-dependent calibration

To examine the applicability of the framework under a contrasting loading speed, an additional calibration was performed at a low displacement speed of 0.01 $\mathrm{mm\,s^{-1}}$ at $T = -15$ °Celsius. Together with the temperature-variation calibrations performed at 1 $\mathrm{mm\,s^{-1}}$, this gives two representative loading rates rather than a full sweep over strain rate. Fig. 19 shows the calibrated stress–strain curves against the experimental measurements for all three loading modes. The simulation results fall within or close to the experimental variability band, indicating that the framework identifies physically consistent bond

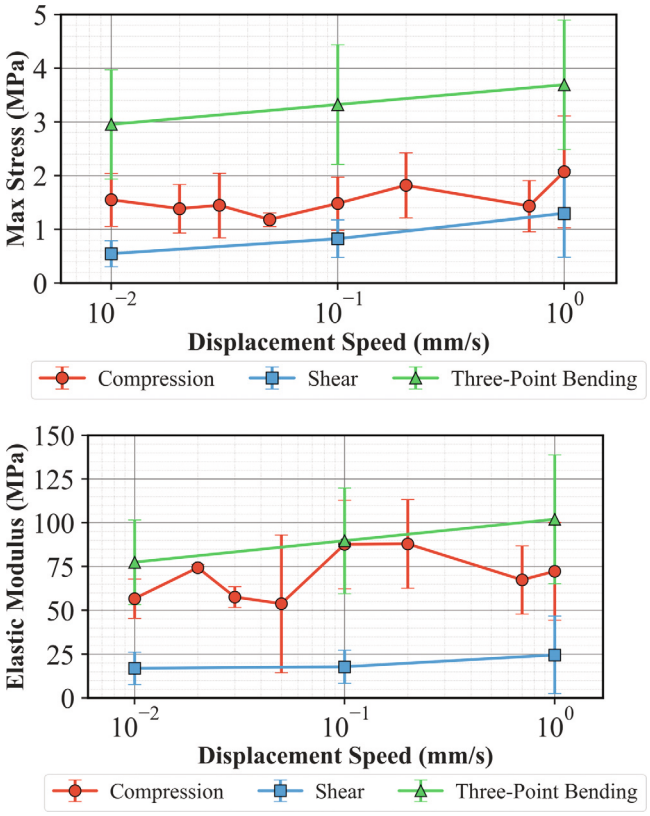

Fig. 10. Effect of displacement speed on peak stress (top) and elastic modulus (bottom) across all three loading modes.

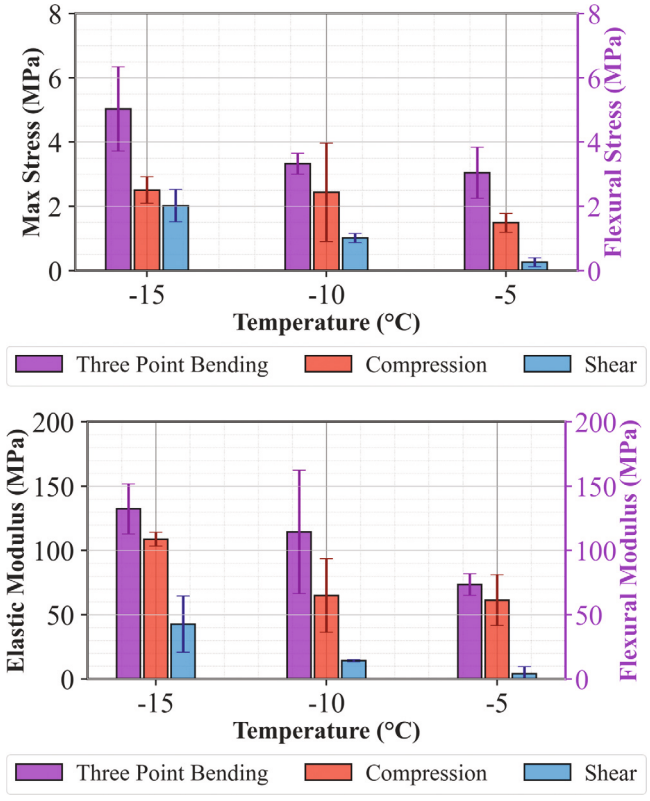

Fig. 11. Effect of temperature on peak stress (top) and elastic modulus (bottom) across all three loading modes.

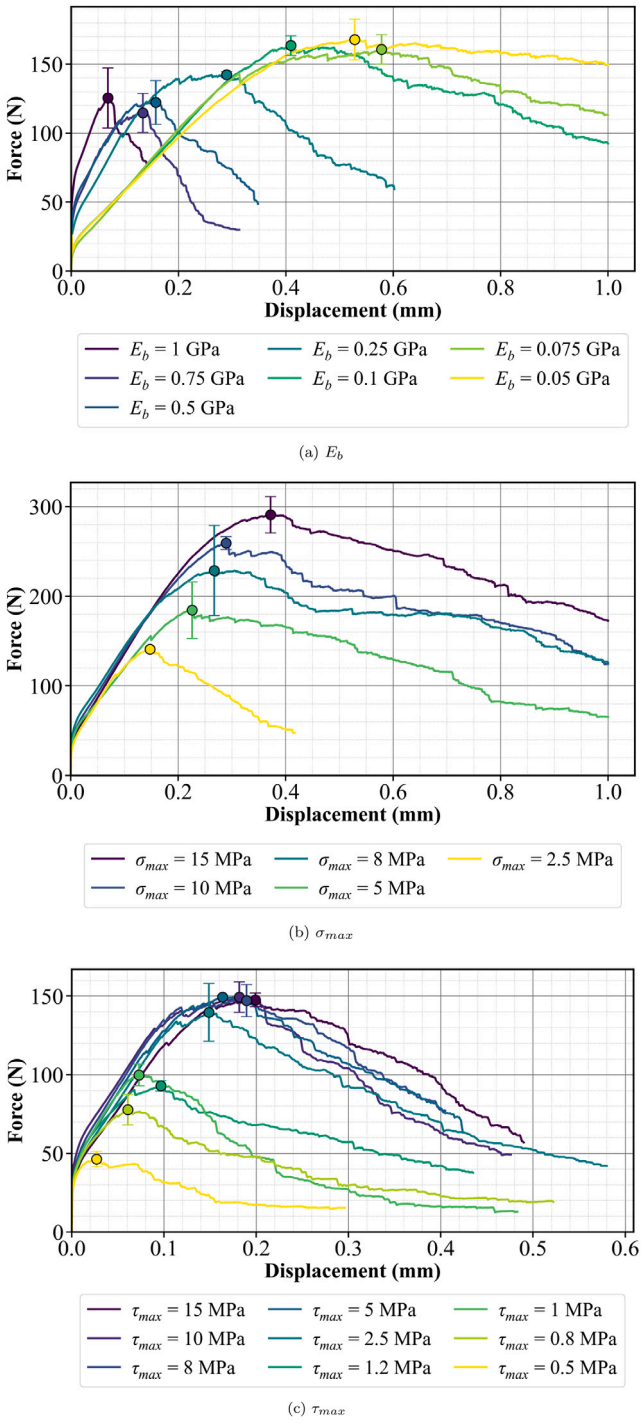

Fig. 12. Force–displacement response when varying each parameter individually: (a) E_b, (b) σ_{max}, and (c) τ_{max}.

parameters at low strain rates as well. Because only two loading rates were considered, the present results should not be interpreted as a complete characterization of rate dependence; additional intermediate rates would be required to identify a continuous rate-dependent parameter law.

Fig. 20 shows the convergence of normalized SSE over iterations. A total SSE reduction of 69% is achieved within 12 optimization iterations, and the remaining residual reflects the same scalarised multi-objective compromise discussed for the temperature cases.

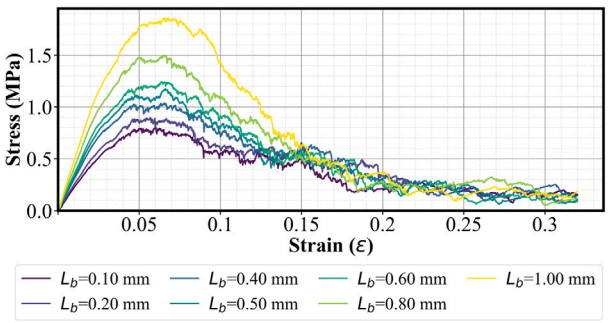

(a) L_b

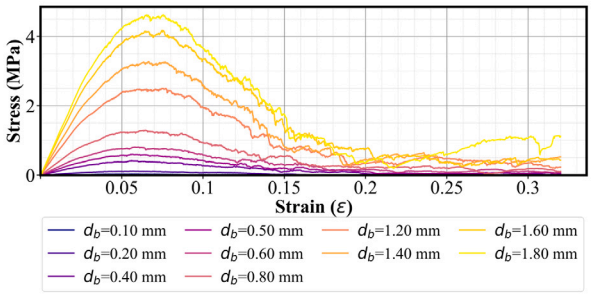

(b) d_b

Fig. 13. Sensitivity of the stress–strain response to structural bond parameters: (a) L_b and (b) d_b, completing the stiffness block alongside E_b.

Table 3
Identified bond parameters from the two-phase calibration for all four cases.

Parameter	Temperature variation (1 mm s^{-1})			Strain-rate variation
	−15 °C	−10 °C	−5 °C	0.01 mm s^{-1} (−15 °C)
Block 1: Stiffness parameters				
E_b (MPa)	10.68	9.68	6.74	5.56
d_b (mm)	1.09	0.99	1.04	0.94
L_b (mm)	1.03	1.03	1.02	1.35
Block 2: Strength parameters				
σ_{max} (MPa)	8.6	2.4	2.3	1.44
τ_{max} (MPa)	0.46	0.55	0.22	0.71
Creep parameters (fixed from global search)				
A (MPa^{-m} s^{-1})	1.5×10^{-10}	1.5×10^{-10}	1.5×10^{-10}	1.5×10^{-10}
m (—)	1	1	1	1

5.3.3. Physical interpretation and framework assessment

The merits of the proposed hybrid framework can be summarized in three points. First, the global Latin-Hypercube phase provides initial estimates close to the optimum and fixes the locally non-identifiable creep parameters at numerically stable values, so that the local refinement operates on a well-conditioned sub-problem and avoids the shallow local minima that trap purely gradient-based methods in this strongly coupled parameter space. Second, the prior-based Tikhonov regularization stabilizes the inherently ill-posed inverse problem: it bounds the Gauss–Newton update, anchors the solution to the physically screened global prior, and lowers the condition number of the regularized normal equations ($\mathbf{X}_b^T\mathbf{X}_b + \mu_b\mathbf{I}$) by two to three orders of magnitude, without biasing physically non-zero parameters toward zero. Third, the strategy is computationally economical, requiring substantially fewer DEM evaluations than population-based optimizers or surrogate-model training, which typically demand hundreds of simulations per configuration.

Across all four calibration cases, the hybrid two-phase framework consistently reduces the discrepancy between DEM simulations and experiments. The experimental rate and temperature dependence is consistent with viscoplastic behavior of the ice-bonded network. In the present inverse model, however, the creep parameters A and m are treated as stability-controlling parameters fixed from the global search, and the condition-specific changes in specimen stiffness and maximum stress (as established in Section 5.1) are mainly absorbed by the calibrated stiffness (E_b, d_b, L_b) and strength (σ_{max}, τ_{max}) parameters. Within this fixed-creep formulation the calibration procedure identifies a condition-specific bond-parameter set for each temperature and loading rate. The calibrated normal strength at $T = -15$ °Celsius is markedly larger than in the $T = -10$ and $T = -5$ °Celsius cases, and the corresponding σ_{max}/τ_{max} ratio is also higher than in the other calibrated cases. Because these are effective meso-scale BPM parameters identified within a fixed-creep formulation, this difference should be interpreted as a compensation effect between stiffness, strength, and the fixed creep parameters rather than as a directly measured ice-bond strength ratio.

The reduced identifiability of the creep parameters can be stated more precisely. Within the numerically stable region selected by the global search, the macroscopic response over the experimental loading times depends only weakly on A and m: local finite-difference perturbations of these parameters produced weak, non-monotonic, and numerically inconsistent changes in the simulated responses, so reliable local sensitivity columns could not be constructed for them, and their simultaneous local identification was ill-conditioned under the available tests. Fixing A and m at the globally screened values therefore removes an ill-conditioned direction from the local problem and improves its conditioning. A direct consequence is the compensation effect noted above: because the viscoplastic contribution is held constant, any temperature- or rate-induced change that the real material would accommodate through creep must instead be absorbed by the calibrated stiffness and strength parameters. The identified σ_{max}, τ_{max}, E_b, d_b, and L_b are therefore *effective* meso-scale quantities that are partially entangled with the fixed creep parameters, and derived ratios such as σ_{max}/τ_{max} should be read as effective calibration outcomes rather than as directly measured ice-bond properties.

The two-phase structure is central to the observed performance. The global search phase eliminates problematic local minima associated with the strongly coupled stiffness parameters (E_b, d_b, L_b) and fixes the creep parameters (A, m) at numerically stable values, so that the local refinement phase operates on a better-conditioned sub-problem that is easier to navigate by gradient-based methods. Without this prior global conditioning, gradient-based local methods applied from arbitrary starting points are prone to becoming trapped in shallow local minima, particularly for the scalarised multi-objective formulation used here, where the sensitivity signatures of individual parameters can partially cancel across tests. The improvement of the total residual across the four calibration cases indicates that the block partition reduces ill-conditioning without preventing the coupled response from being fitted, even though the two blocks are weakly coupled rather than strictly independent.

The remaining residual error after calibration is an inherent consequence of the scalarised multi-objective formulation. A single parameter set must simultaneously minimize mismatch across three tests that activate fundamentally different failure mechanisms. Because the three objective contributions cannot all be driven to zero by a single parameter set, the solution minimizes the aggregate weighted residual across the three tests while maintaining physical consistency across all loading modes. This is not a shortcoming of the method, but a physically correct outcome. The identified parameters represent the bond properties that explain all three measurements jointly.

Finally, it is worth emphasizing that the aim of the present framework is not to force a single, strictly unique parameter set, but to identify a physically consistent set that is jointly compatible with all three loading modes. Because the inverse problem remains non-unique, aiming for strict uniqueness, for example by over-fitting a single test or by treating the calibrated values as exact material constants, could place the solution at an arbitrary point of the admissible region and

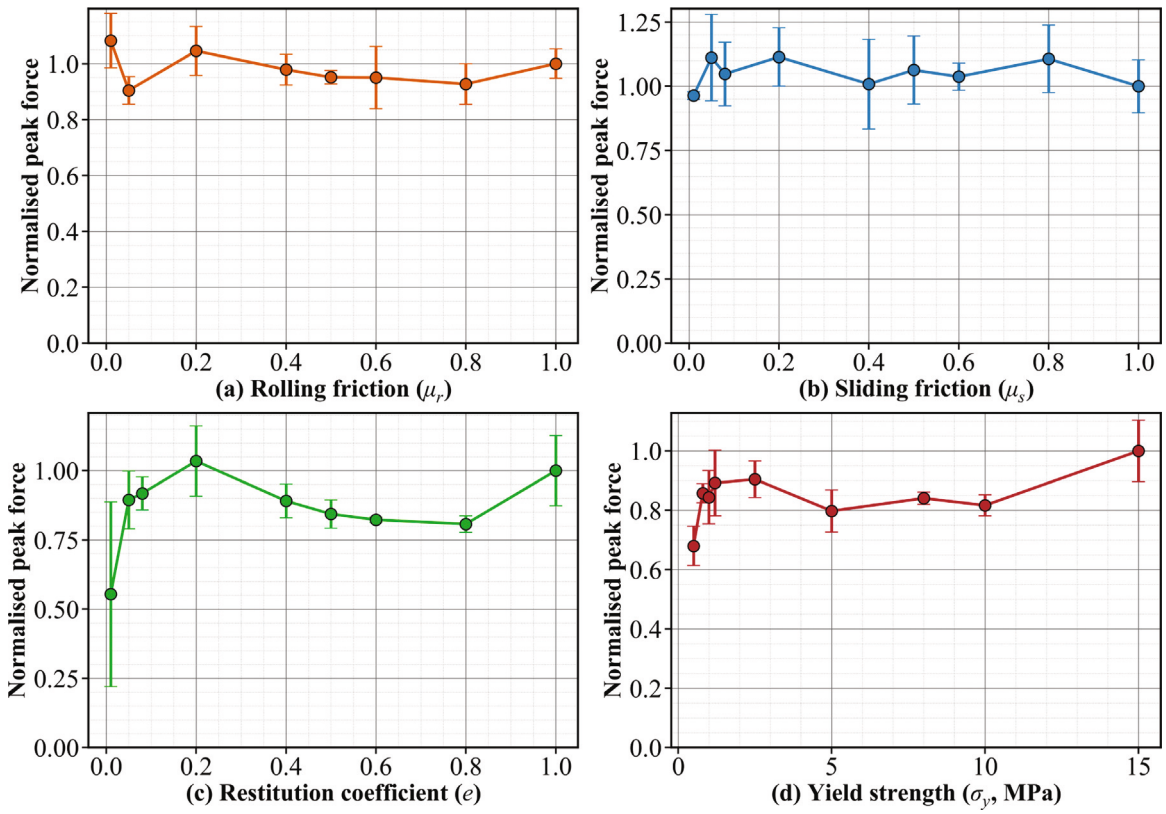

Fig. 14. Effect of non-significant DEM contact parameters ((a)rolling friction μ_r, (b) sliding friction μ_s, (c) restitution factor e) and (d) yield strength σ_y on normalized peak force. Each curve represents the mean peak force from three replicate simulations, normalized by the value at the highest tested parameter level.

could therefore yield overly optimistic or overly pessimistic predictions when the model is applied beyond the calibrated conditions. The envelope-aware formulation mitigates this risk, because it accepts the family of parameter sets whose responses lie within the experimental scatter band rather than committing to one particular point estimate.

6. Conclusions

This study introduced a hybrid two-phase inverse calibration framework for meso-scale bond parameters in bonded-particle model simulations of frozen particle-fluid systems. A Taguchi L_{32} screening identified five significant parameters and fixed the locally non-identifiable creep parameters at numerically stable values, after which an alternating block-minimization algorithm with prior-based Tikhonov regularization refined the stiffness and strength blocks against uniaxial compression, three-point bending, and shear simultaneously. Application to frozen glass-bead specimens at three temperatures and two representative loading rates yielded SSE reductions of 28%–95% per condition, with condition-specific parameter sets whose trends are consistent with the observed rate- and temperature-dependent response.

The work addresses inverse identification and calibration consistency rather than predictive transfer. We emphasize that the predictive capability of the framework beyond the calibrated conditions has not been demonstrated: each temperature and loading rate is calibrated independently, and the present results do not establish that a parameter set identified at one condition can predict the response at an unseen condition. Several directions are left for future work, since they require additional experiments. For example, the framework could be extended to unseen temperatures or strain rates through a hold-out validation in which an intermediate condition is predicted from calibrations at the bounding conditions. Moreover, a temperature- and rate-dependent creep law could be identified, and the framework could subsequently be applied to natural frozen soils.

The three loading modes were weighted equally ($w_L = 1$) in the present study, because compression, three-point bending, and shear activate different dominant mechanisms and were therefore regarded as equally informative, with no loading mode given priority. This is a neutral default, and the calibrated parameter set may change under a different weighting. Several principled weighting strategies are available for future applications: weighting each test by the inverse variance of its experimental data, so that more reproducible measurements carry greater influence; weighting by the engineering relevance of each loading mode for the intended application; or replacing the scalarised weighted sum with a Pareto-based multi-objective formulation that identifies the trade-off front directly and thereby avoids subjective weights altogether. It should be noted, however, that adding further experiments does not necessarily improve parameter identification: a new test is beneficial only when it provides information that is complementary to, rather than redundant with, the existing tests. For this reason, the information content of a candidate test can be assessed before calibration. For example, Mostafaei et al. [50] applied a data-driven principal-component analysis to determine which DEM characterization tests carry the most information for the target bulk behavior; the same approach can be transferred to the present framework to decide whether an additional experiment provides genuinely new information for BPM bond-parameter calibration before it is included and weighted.

Within these limits, the framework offers a computationally efficient and physically interpretable alternative to trial-and-error and surrogate-based BPM calibration.

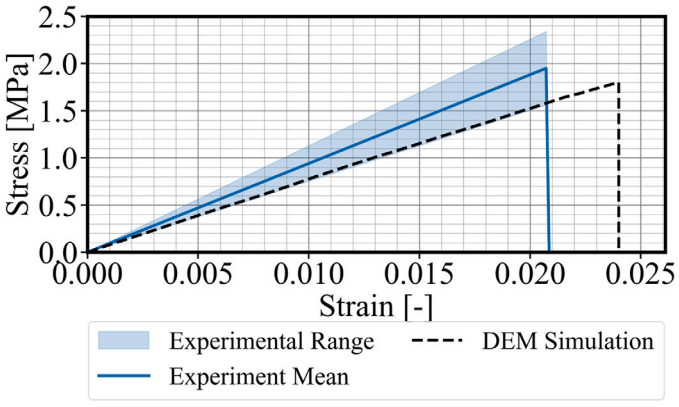

(a) Uniaxial compression test

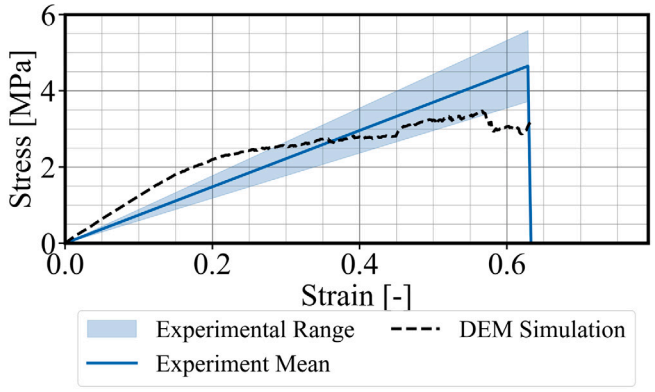

(b) Three-point bending test

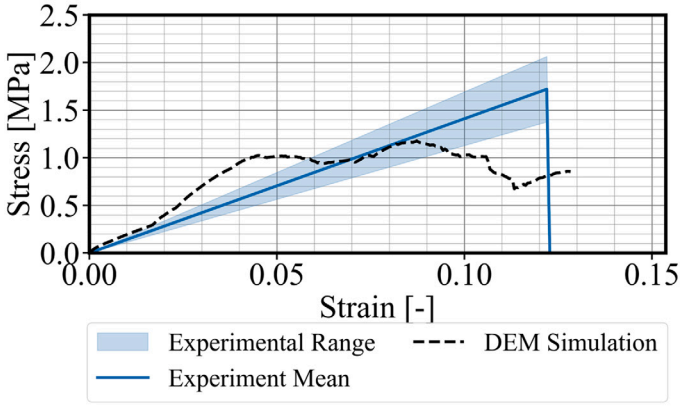

(c) Shear test

Fig. 15. Calibrated DEM simulation versus experimental stress–strain curves at $T = -15$ °Celsius. The shaded band represents experimental variability across repeated tests.

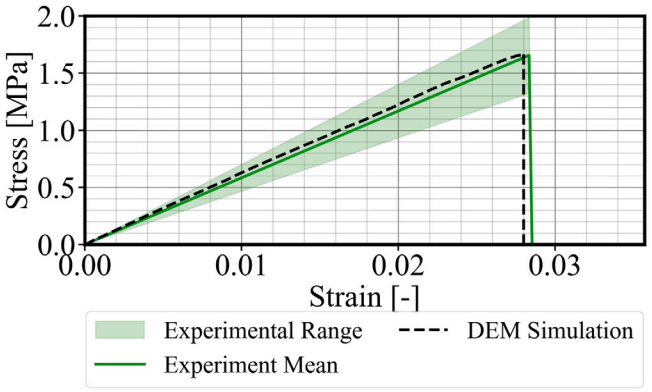

(a) Uniaxial compression test

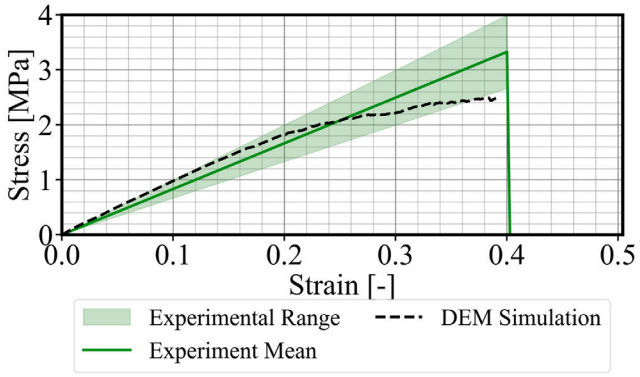

(b) Three-point bending test

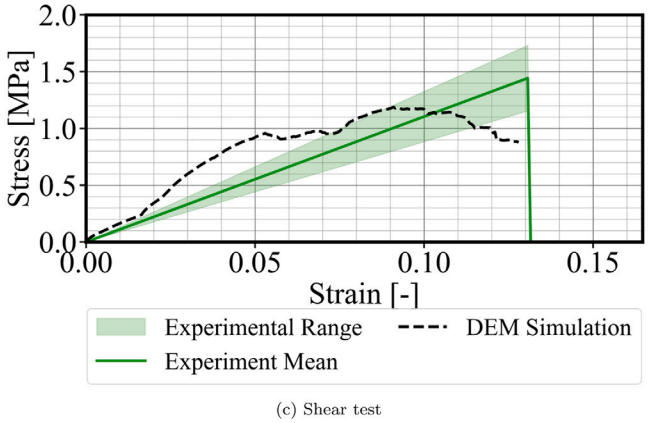

(c) Shear test

Fig. 16. Calibrated DEM simulation versus experimental stress–strain curves at $T = -10$ °Celsius.

CRediT authorship contribution statement

Amirali Khosrozadeh: Writing – original draft, Visualization, Validation, Software, Methodology, Investigation, Formal analysis, Data curation, Conceptualization. **Amir Khosravifard:** Writing – review & editing, Software, Methodology. **Swantje Pietsch-Braune:** Writing – review & editing, Software, Methodology. **Stefan Heinrich:** Writing – review & editing, Supervision, Resources, Project administration, Funding acquisition.

Declaration of Generative AI and AI-assisted technologies in the writing process

During the preparation of this work, the authors used Claude and ChatGPT to improve the readability of the manuscript by rearranging and rewording sentences, and used ChatGPT to assist with the design of the graphical images. After using these tools, the authors carefully reviewed and edited the content as necessary and take full responsibility for the content of the published article.

Declaration of competing interest

The authors declare that they have no known competing financial interests or personal relationships that could have appeared to influence the work reported in this paper.

Acknowledgments

The authors gratefully acknowledge funding from the German Research Foundation (DFG) under project number HE-4526/40-1.

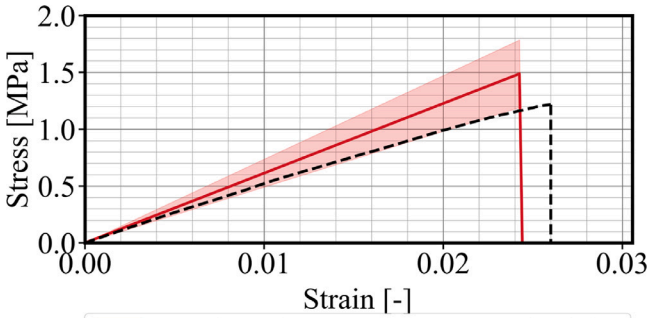

(a) Uniaxial compression test

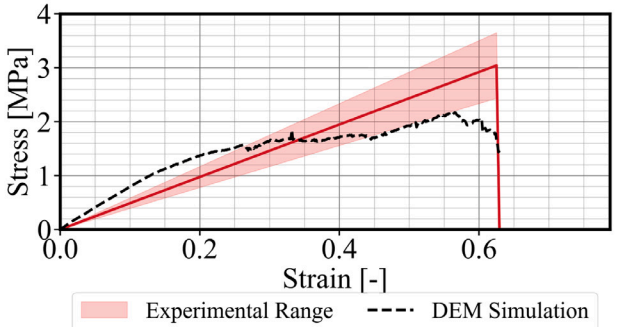

(b) Three-point bending test

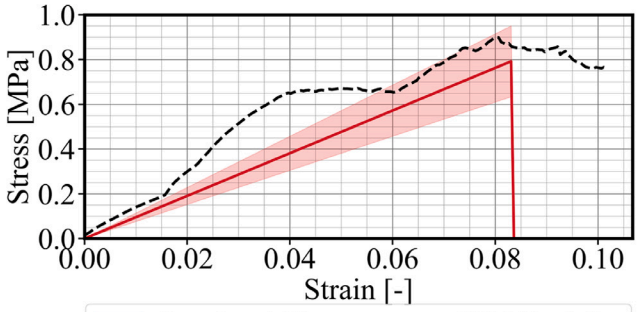

(c) Shear test

Fig. 17. Calibrated DEM simulation versus experimental stress–strain curves at $T = -5$ °Celsius.

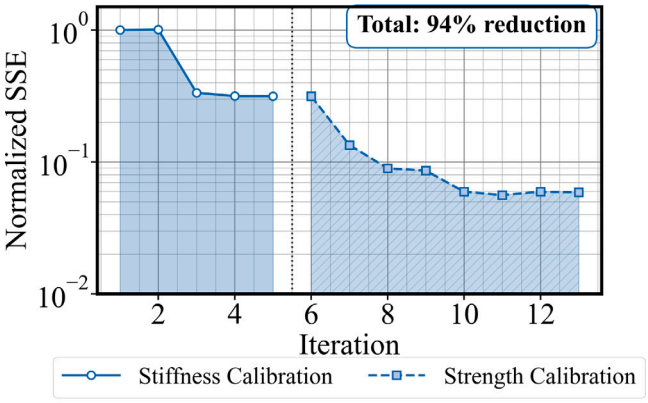

(a) $T = -15$ °C

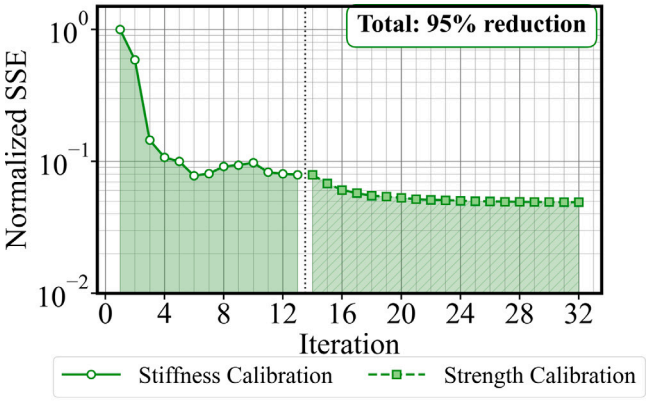

(b) $T = -10$ °C

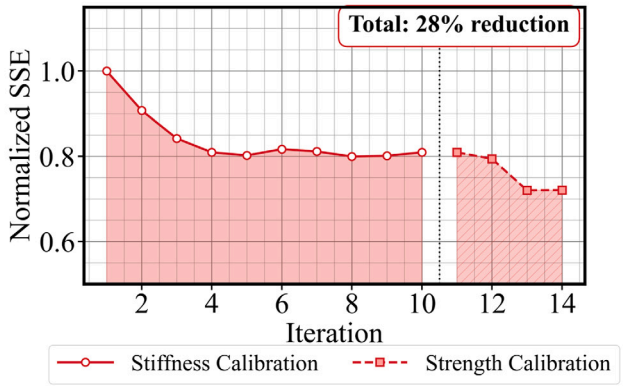

(c) $T = -5$ °C

Fig. 18. Convergence of normalized $\widehat{\text{SSE}}$ during the two-phase calibration at the three calibrated temperatures.

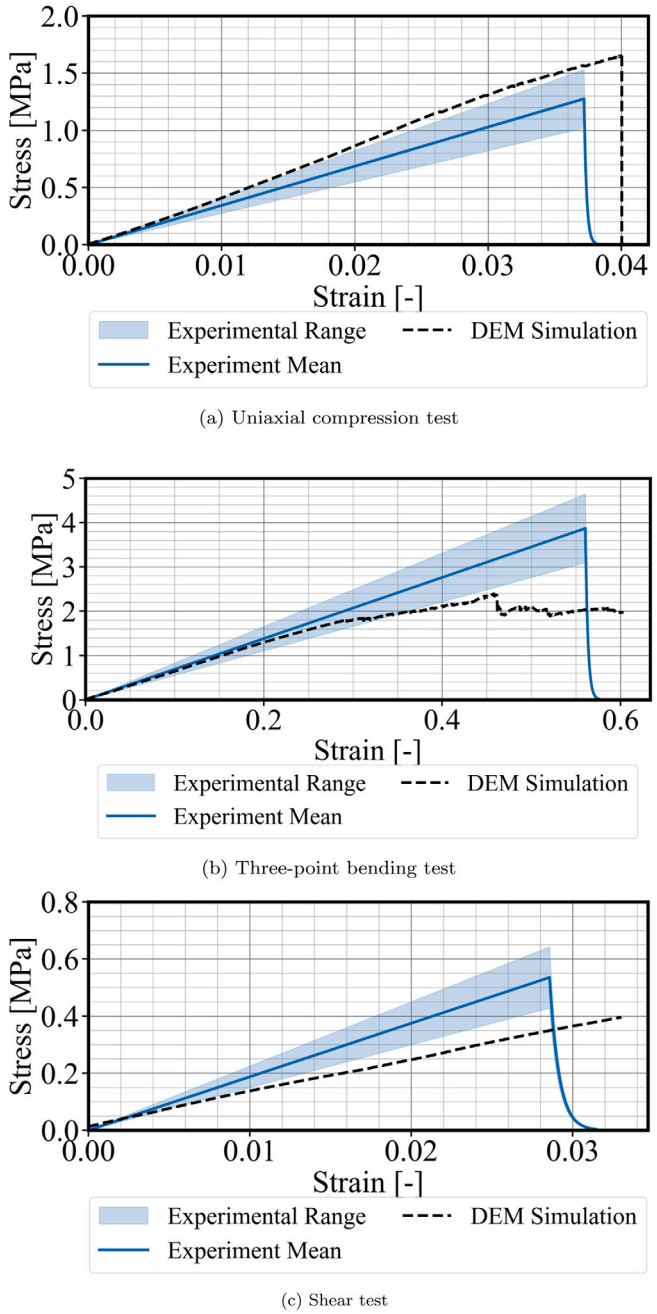

Fig. 19. Calibrated DEM simulation versus experimental stress–strain curves at 0.01 mm s^{-1} and $T = -15$ °Celsius. The shaded band represents experimental variability across repeated tests.

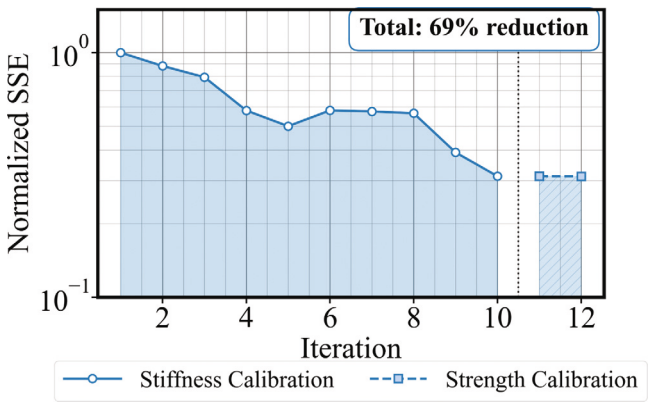

Fig. 20. Convergence of normalized SSE during the two-phase calibration at 0.01 mm s^{-1}, $T = -15$ °Celsius.

Appendix A. Analysis of variance (ANOVA) tables from DOE study

This appendix presents the complete ANOVA results from the Taguchi L_{32} design of experiments study for the three mechanical tests: uniaxial compression, shear, and three-point bending. These statistical analyses quantify the significance of each parameter's influence on the maximum force response, providing the basis for parameter selection in the inverse characterization framework.

A.1. Uniaxial compression test ANOVA

Table A.1 presents the ANOVA results for the uniaxial compression test.

Table A.1
ANOVA table for uniaxial compression test (Response: Maximum Force).

Source	SS	df	MS	F	p-value
Model	3 321 000	28	118 600	11.13	**0.0039**
E_b	332 200	3	110 700	10.39	**0.0430**
σ_{max}	1 783 000	3	594 300	55.75	**0.0039**
τ_{max}	700 400	3	233 500	21.90	**0.0153**
σ_y	8225.43	3	2741.81	0.26	0.8529
e	11 069.05	1	11 069.05	1.04	0.3832
μ_s	16 409.33	3	5469.78	0.51	0.7013
μ_r	34 537.61	3	11 512.54	1.08	0.4755
ϵ_f	154 400	3	51 460.60	4.83	0.1143
A	213 700	3	71 233.08	6.68	0.0765
m	67 401.60	3	22 467.20	2.11	0.2780
Residual	31 980.83	3	10 660.28	–	–
Cor Total	3 353 000	31	–	–	–

Fit Statistics: $R^2 = 0.9905$; Adj. $R^2 = 0.9014$; Pred. $R^2 = -0.0851$; Adeq. Prec. = 14.18
Note: Bold p-values indicate statistically significant factors ($p < 0.05$)

Table A.2
ANOVA table for shear test (Response: Maximum Force).

Source	SS	df	MS	F	p-value
Model	3175.18	25	127.01	4.56	**0.0331**
E_b	317.23	1	317.23	11.38	**0.0150**
σ_{max}	168.34	3	56.11	2.01	0.2136
τ_{max}	156.71	3	52.24	1.87	0.2348
σ_y	35.16	3	11.72	0.42	0.7451
e	178.35	3	59.45	2.13	0.1973
μ_s	131.35	3	43.78	1.57	0.2914
μ_r	80.02	3	26.67	0.96	0.4711
A	993.06	3	331.02	11.88	**0.0062**
m	1114.96	3	371.65	13.34	**0.0046**
Residual	167.20	6	27.87	–	–
Cor Total	3342.38	31	–	–	–

Fit Statistics: $R^2 = 0.9500$; Adj. $R^2 = 0.7415$; Pred. $R^2 = -0.4229$; Adeq. Prec. = 6.28
Note: Bold p-values indicate statistically significant factors ($p < 0.05$).

A.2. Shear test ANOVA

Table A.2 shows the ANOVA results for the shear test.

A.3. Three-point bending test ANOVA

Table A.3 presents the ANOVA results for the three-point bending test.

A.4. Summary of parameter significance across all tests

The ANOVA results consistently identify five parameters as statistically significant or approaching significance across multiple loading

Table A.3
ANOVA table for three-point bending test (Response: Maximum Force).

Source	SS	df	MS	F	p-value
Model	1297.07	28	46.32	11.29	**0.0343**
E_b	98.75	1	98.75	24.07	**0.0162**
σ_{max}	107.30	3	35.77	8.72	0.0543
τ_{max}	33.24	3	11.08	2.70	0.2181
σ_y	9.71	3	3.24	0.79	0.5749
e	59.16	3	19.72	4.81	0.1148
μ_s	26.94	3	8.98	2.19	0.2683
μ_r	20.91	3	6.97	1.70	0.3370
ϵ_f	48.78	3	16.26	3.96	0.1439
A	434.66	3	144.89	35.31	**0.0077**
m	457.62	3	152.54	37.18	**0.0071**
Residual	12.31	3	4.10	–	–
Cor Total	1309.38	31	–	–	–

Fit Statistics: $R^2 = 0.9906$; Adj. $R^2 = 0.9029$; Pred. $R^2 = -0.0695$; Adeq. Prec. = 9.52
Note: Bold p-values indicate statistically significant factors ($p < 0.05$)

Table A.4
Summary of p-values for all parameters across mechanical tests.

Parameter	Compression	Shear	Bending
Selected parameters:			
E_b	**0.043****	**0.015****	**0.016****
σ_{max}	**0.004*****	0.214	0.054*
τ_{max}	**0.015****	0.235	0.218
A	0.077*	**0.006*****	**0.008*****
m	0.278	**0.005*****	**0.007*****
Not selected:			
σ_y	0.853	0.745	0.575
e	0.383	0.197	0.115
μ_s	0.701	0.291	0.268
μ_r	0.476	0.471	0.337
ϵ_f	0.114	–	–

*** p < 0.01
** p < 0.05
* p < 0.10
Selected parameters show significance in 1–3 tests, with E_b and creep parameters significant in all tests, explaining >95% of response variance.

Table B.1
Complete Taguchi L_{32} orthogonal array with responses from compression, bending, and shear tests.

Run	Parameter levels										Compression		Bending		Shear	
	E_b (MPa)	σ_n (MPa)	σ_t (MPa)	σ_y (MPa)	e (-)	μ_s (-)	μ_r (-)	ϵ_f (-)	A (-)	m (-)	F_{max} (N)	Stiff. (N/mm)	F_{max} (N)	Stiff. (N/mm)	F_{max} (N)	Stiff. (N/mm)
1	100	1.0	0.5	5.0	0.1	0.1	0.01	0.01	0.01	0.05	245	1850	182	1425	98	1120
2	100	8.0	7.0	10.0	0.3	0.3	0.03	0.03	0.34	0.20	512	2150	395	1680	285	1450
3	100	16.0	13.5	15.0	0.5	0.5	0.05	0.05	0.67	0.35	825	2580	645	2050	495	1825
4	100	25.0	20.0	20.0	0.7	0.7	0.07	0.07	1.0	0.50	1145	2950	892	2385	715	2150
5	200	1.0	7.0	15.0	0.1	0.3	0.05	0.07	0.67	0.50	385	3250	295	2580	215	2050
6	200	8.0	0.5	20.0	0.3	0.1	0.07	0.05	1.0	0.35	625	3685	485	2950	165	2425
7	200	16.0	20.0	5.0	0.5	0.7	0.01	0.03	0.01	0.20	1385	4150	1085	3380	825	2850
8	200	25.0	13.5	10.0	0.7	0.5	0.03	0.01	0.34	0.05	1725	4625	1365	3785	1045	3285
9	350	1.0	13.5	20.0	0.1	0.5	0.07	0.03	0.34	0.50	565	5825	445	4650	385	3850
10	350	8.0	20.0	15.0	0.3	0.7	0.05	0.01	0.01	0.35	1545	6350	1225	5125	945	4385
11	350	16.0	0.5	10.0	0.5	0.1	0.03	0.07	1.0	0.20	1125	6925	885	5625	285	4950
12	350	25.0	7.0	5.0	0.7	0.3	0.01	0.05	0.67	0.05	2185	7485	1745	6150	1325	5485
13	500	1.0	20.0	10.0	0.1	0.7	0.03	0.05	1.0	0.20	1285	8350	1025	6850	825	5950
14	500	8.0	13.5	5.0	0.3	0.5	0.01	0.07	0.67	0.05	1825	8925	1465	7385	1145	6585
15	500	16.0	7.0	20.0	0.5	0.3	0.07	0.01	0.01	0.50	2465	9525	1985	7950	1485	7225
16	500	25.0	0.5	15.0	0.7	0.1	0.05	0.03	0.34	0.35	2125	10 150	1685	8525	485	7885
17	100	1.0	20.0	15.0	0.5	0.5	0.03	0.07	0.34	0.35	485	2250	375	1785	295	1385
18	100	8.0	13.5	20.0	0.7	0.7	0.01	0.05	0.01	0.50	785	2685	615	2125	485	1725
19	100	16.0	7.0	5.0	0.1	0.1	0.07	0.03	1.0	0.05	1025	3125	815	2485	625	2085
20	100	25.0	0.5	10.0	0.3	0.3	0.05	0.01	0.67	0.20	685	3585	525	2850	185	2465
21	200	1.0	13.5	5.0	0.5	0.7	0.05	0.01	0.67	0.20	745	4285	585	3425	485	2885
22	200	8.0	20.0	10.0	0.7	0.5	0.07	0.03	1.0	0.05	1625	4785	1285	3885	1025	3325
23	200	16.0	0.5	15.0	0.1	0.3	0.01	0.05	0.01	0.50	1185	5325	925	4350	285	3785
24	200	25.0	7.0	20.0	0.3	0.1	0.03	0.07	0.34	0.35	2025	5885	1625	4825	1245	4265
25	350	1.0	7.0	10.0	0.5	0.3	0.07	0.05	0.01	0.35	825	7125	645	5785	525	4885

(*continued on next page*)

Table B.1 (*continued*).

26	350	8.0	0.5	5.0	0.7	0.1	0.05	0.07	0.34	0.20	1085	7685	845	6285	285	5425
27	350	16.0	20.0	20.0	0.1	0.7	0.03	0.01	1.0	0.05	2625	8285	2125	6825	1685	5985
28	350	25.0	13.5	15.0	0.3	0.5	0.01	0.03	0.67	0.50	2985	8925	2425	7385	1925	6585
29	500	1.0	0.5	20.0	0.5	0.1	0.01	0.03	0.34	0.05	865	9825	675	8125	285	7285
30	500	8.0	7.0	15.0	0.7	0.3	0.03	0.01	0.01	0.20	2125	10 485	1725	8725	1385	7925
31	500	16.0	13.5	10.0	0.1	0.5	0.05	0.07	1.0	0.35	2885	11 185	2345	9325	1825	8585
32	500	25.0	20.0	5.0	0.3	0.7	0.07	0.05	0.67	0.50	3585	11 925	2925	9950	2385	9265

conditions. Table A.4 summarizes the p-values for each parameter across all three tests, demonstrating the systematic selection of the five most influential parameters.

In contrast, the remaining parameters show no significant effect in any test (yield strength, restitution coefficient, sliding friction, rolling friction, fracture strain). These parameters can be assigned literature values or calibrated separately through simpler auxiliary tests, thereby reducing the dimensionality and improving the conditioning of the inverse problem.

Appendix B. Complete Taguchi L_{32} experimental runs

This appendix presents the complete Taguchi L_{32} orthogonal array with all parameter combinations and corresponding response values from the three mechanical tests (see Table B.1).

Data availability

Data will be made available on request.

References

[1] P. Cundall, R. Hart, Numerical modelling of discontinua, Eng. Comput. 9 (2) (1992) 101–113.

[2] D. Potyondy, P. Cundall, A bonded-particle model for rock, Int. J. Rock Mech. Min. Sci. 41 (8) (2004) 1329–1364.

[3] T. Kazerani, J. Zhao, Micromechanical parameters in bonded particle method for modelling of brittle material failure, Int. J. Numer. Anal. Methods Geomech. 34 (18) (2010) 1877–1895.

[4] M. Dosta, T. Chan, Linking process-property relationships for multicomponent agglomerates using dem-ann-pbm coupling, Powder Technol. 398 (2022) 117156, http://dx.doi.org/10.1016/j.powtec.2022.117156.

[5] D. Potyondy, The bonded-particle model as a tool for rock mechanics research and application: current trends and future directions, Geosystem Eng. 18 (1) (2015) 1–28, http://dx.doi.org/10.1080/12269328.2014.998346.

[6] M. Nitka, J. Tejchman, Modelling of concrete behaviour in uniaxial compression and tension with dem, Granul. Matter 17 (2015) 145–164, http://dx.doi.org/10.1007/s10035-015-0546-4.

[7] S. Ji, S. Di, X. Long, Dem simulation of uniaxial compressive and flexural strength of sea ice: parametric study, J. Eng. Mech. 143 (1) (2017) C4016010.

[8] L. Arenson, S. Springman, D. Sego, The rheology of frozen soils, Appl. Rheol. 17 (1) (2007) 12147–1–12147–14, http://dx.doi.org/10.1515/arh-2007-0003.

[9] U. Schindler, S. Chrisopoulos, R. Cudmani, Artificial ground freezing applications using an advanced elastic-viscoplastic model for frozen granular soils, Cold Reg. Sci. & Technol. 215 (2023) 103964.

[10] S. Deville, Freezing colloids: Observations, Principles, Control, and Use: Applications in Materials Science, Life Science, Earth Science, Food Science and Engineering, Springer, 2017, http://dx.doi.org/10.1007/978-3-319-50515-2.

[11] H. Song, P. Verdin, J. Zhang, Research developments and applications of ice slurry, Energies 17 (20) (2024) 5213, http://dx.doi.org/10.3390/en17205213.

[12] P. Nikolaev, A. Jivkov, L. Margetts, M. Sedighi, Modelling artificial ground freezing subjected to high velocity seepage, Int. J. Heat Mass Transfer 221 (2024) 125084.

[13] A. Sweidan, K. Niggemann, Y. Heider, M. Ziegler, Experimental study and numerical modeling of the thermo-hydro-mechanical processes in soil freezing with different frost penetration directions, Acta Geotech. 17 (2022) 231–255.

[14] S. Sjölind, A constitutive model for ice as a damaging visco-elastic material, Cold Reg. Sci. & Technol. 14 (3) (1987) 247–262.

[15] S. Chehreghani, M. Noaparast, B. Rezai, S. Shafaei, Bonded-particle model calibration using response surface methodology, Particuology 32 (2017) 141–152.

[16] M. Wu, A. Hu, S. Zhou, X. Mao, F. Wang, Research on calibration method of microscopic parameters of siltstone based on gray theory, Sci. Rep. 13 (2023) 15802.

[17] Y. Wang, F. Tonon, Calibration of a discrete element model for intact rock up to its peak strength, Int. J. Numer. Anal. Methods Geomech. 34 (2010) 447–469, http://dx.doi.org/10.1002/nag.811.

[18] A. Fakhimi, T. Villegas, Application of dimensional analysis in calibration of a discrete element model for rock deformation and fracture, Rock Mech. Rock Eng. 40 (2007) 193–211, http://dx.doi.org/10.1007/s00603-006-0095-6.

[19] J. Zhang, Y. Chen, R. Du, Z. Huang, X. Zhao, Experimental study and numerical simulation verification of the macro- and micromechanical properties of the sandstone–concrete interface under freeze–thaw cycles, Constr. Build. Mater. (2024) http://dx.doi.org/10.1016/j.conbuildmat.2024.136584.

[20] J. Yoon, Application of experimental design and optimization to pfc model calibration in uniaxial compression simulation, Int. J. Rock Mech. Min. Sci. 44 (2007) 871–889, http://dx.doi.org/10.1016/j.ijrmms.2007.01.004.

[21] K. Hanley, C. O'Sullivan, J. Oliveira, K. Cronin, E. Byrne, Application of taguchi methods to dem calibration of bonded agglomerates, Powder Technol. 210 (2011) 230–240, http://dx.doi.org/10.1016/j.powtec.2011.03.023.

[22] K. Jarolin, S. Doose, W. Kurtz, A. Katterfeld, Linearization-based methods for the calibration of bonded-particle models, Comput. Part. Mech. 8 (2020) 511–527.

[23] L. Benvenuti, C. Kloss, S. Pirker, Identification of dem simulation parameters by artificial neural networks and bulk experiments, Powder Technol. 291 (2016) 456–465, http://dx.doi.org/10.1016/j.powtec.2016.01.003.

[24] F. Salazar J. Irazábal, D. Vicente, A methodology for calibrating parameters in discrete element models based on machine learning surrogates, Comput. Part. Mech. 10 (2023) 1031–1047, http://dx.doi.org/10.1007/s40571-022-00550-1.

[25] H. Cheng, T. Shuku, K. Thoeni, P. Tempone, S. Luding, V. Magnanimo, An iterative bayesian filtering framework for fast and automated calibration of dem models, Comput. Methods Appl. Mech. Engrg. 350 (2019) 268–294.

[26] Y. Ni, X. Leng, R. Wang, F. Xia, F. Wang, C. Wang, A dem parameter calibration method based on bp neural network and genetic algorithm, Int. J. Numer. Anal. Methods Geomech. 49 (2025) 3897–3916, http://dx.doi.org/10.1002/nag.70043.

[27] S. Long, S. Xu, Y. Zhang, B. Li, L. Sun, Y. Wang, J. Wang, Method of soil-elastoplastic dem parameter calibration based on recurrent neural network, Powder Technol. 416 (2023) 118222, http://dx.doi.org/10.1016/j.powtec.2023.118222.

[28] M. Wang, P. Cao, Calibrating micro-parameters of PFC2D(3D) model using the improved simulated annealing algorithm, Math. Probl. Eng. 2 017 (2017) 6401835.

[29] M. Wang, Z. Lu, Y. Zhao, W. Wan, Calibrating microparameters of DEM models by using CEM,DE, EFO, MFO,SSO algorithms and the optimal hyperparameters, Comput. Part. Mech. 11 (2024) 839–852.

[30] M. Wang, Z. Lu, Y. Zhao, W. Wan, A calibration framework for DEM models based on the stress–strain curve of uniaxial compressive tests by using the AEO algorithm and several calibration suggestions, Comput. Part. Mech. 12 (2025) 541–555.

[31] H. Cheng, T. Shuku, K. Thoeni, H. Yamamoto, Probabilistic calibration of discrete element simulations using the sequential quasi-monte carlo filter, Granul. Matter 20 (1) (2018) 11, http://dx.doi.org/10.1007/s10035-017-0781-y.

[32] H. Do, D. Schott A. Aragón, A calibration framework for discrete element model parameters using genetic algorithms, Adv. Powder Technol. 29 (2018) 1393–1403, http://dx.doi.org/10.1016/j.apt.2018.03.001.

[33] M. Wang, Z. Lu, W. Wan, Y. Zhao, A calibration framework for the microparameters of the dem model using the improved pso algorithm, Adv. Powder Technol. 32 (2021) 358–369, http://dx.doi.org/10.1016/j.apt.2020.12.015.

[34] T. Qu, Y. Feng, M. Wang, S. Jiang, Calibration of parallel bond parameters in bonded particle models via physics-informed adaptive moment optimisation, Powder Technol. 366 (2020) 527–536, http://dx.doi.org/10.1016/j.powtec.2020.02.077.

[35] C. Richter, G. Kunze T. Rößler, A. Katterfeld, F. Will, Development of a standard calibration procedure for the dem parameters of cohesionless bulk materials—part ii: Efficient optimization-based calibration, Powder Technol. 360 (2020) 967–976, http://dx.doi.org/10.1016/j.powtec.2019.10.052.

[36] T. Qu, Y. Feng, T. Zhao, M. Wang, Calibration of linear contact stiffnesses in discrete element models using a hybrid analytical-computational framework, Powder Technol. 356 (2019) 795–807, http://dx.doi.org/10.1016/j.powtec.2019.09.016.

[37] T. Qu, Y. Feng, T. Zhao, M. Wang, A hybrid calibration approach to hertz-type contact parameters for discrete element models, Int. J. Numer. Anal. Methods Geomech. 44 (2020) 1281–1300, http://dx.doi.org/10.1002/nag.3061.

[38] R. Chen, Identification of Discrete Element Model Parameters of Brittle Material by an Inverse Approach (Ph. D. thesis), 2017.

[39] H. Xu, B. Putsikai, S. Yu, J. Yu, Y. Li, P. Gu, Numerical simulation of freezing-induced crack propagation in fractured rock masses under water–ice phase change using discrete element method, Buildings 15 (2025) 2055, http://dx.doi.org/10.3390/buildings15122055.

[40] T. Chan, S. Heinrich, J. Grabe, M. Dosta, Microscale modeling of frozen particle fluid systems with a bonded-particle model method, Materials 15 (2022) 8505, http://dx.doi.org/10.3390/ma15238505.

[41] P. Cundall, O. Strack, A discrete numerical model for granular assemblies, Géotechnique 29 (1) (1979) 47–65.

[42] M. Dosta, V. Skorych, Musen: An open-source framework for gpu-accelerated dem simulations, SoftwareX 12 (2020) 100618.

[43] A. Di Renzo, F. Di Maio, An improved integral non-linear model for the contact of particles in distinct element simulations, Chem. Eng. Sci. 60 (2005) 1303–1312, http://dx.doi.org/10.1016/j.ces.2004.10.004.

[44] K.J. Hanley, C. O'Sullivan, J.C. Oliveira, K. Cronin, E.P. Byrne, Application of taguchi methods to dem calibration of bonded agglomerates, Powder Technol. 210 (3) (2011) 230–240, http://dx.doi.org/10.1016/j.powtec.2011.03.023.

[45] M. McKay, R. Beckman, W. Conover, A comparison of three methods for selecting values of input variables in the analysis of output from a computer code, Technometrics 21 (2) (1979) 239–245.

[46] Y. Wang, G. Wang, S. Wu, Z. Liu, Y. Fang, A calibration method for ore bonded particle model based on deep learning neural network, Powder Technol. 420 (2023) 118417, http://dx.doi.org/10.1016/j.powtec.2023.118417.

[47] A. Tikhonov, V. Arsenin, Solutions of Ill-Posed Problems, Winston and Sons, Washington D. C, 1977.

[48] A. Khosravifard, M. Hematiyan, Inverse analysis of solidification problems using the mesh-free radial point interpolation method, Comput. Model. Eng. Sci. 78 (2011) 185–208.

[49] A. Khosrozadeh, A. Khosravifard, I. Rajabi, Inverse identification of material constants of various cohesive laws for delamination of composites using experimental results, Compos. Struct. 303 (2023) 116241, http://dx.doi.org/10.1016/j.compstruct.2022.116241.

[50] F. Mostafaei, J.G. Khinast, T. Forgber, Selecting effective powder characterization tests for reliable estimation of bin blending performance, Powder Technol. 456 (2025) 120790, http://dx.doi.org/10.1016/j.powtec.2025.120790.